Unevenly Spaced Time Series Analysis: GRS 1758−258

Masterarbeit aus der Physik
vorgelegt von

Maria Hirsch

29. 01. 2014

Dr. Karl Remeis-Sternwarte Bamberg
Erlangen Centre for Astroparticle Physics
Friedrich-Alexander-Universität
Erlangen-Nürnberg

Betreuer: Prof. Dr. Jörn Wilms

Contents

Abstract

This work gives attention to the variability of Galactic black hole binaries. In such systems, the black hole accretes matter from its companion, whose spectral type defines the accretion mechanism to either Roche lobe overflow or (focused) stellar wind accretion. Infalling matter forms an accretion disk, whose geometry strongly influences the X-ray spectral form of the compact object. Observations show black holes' spectral states varying with time. Combined with information about the binary systems orbit and companion, it is possible to learn more about the accretion geometry and to test the different available models.

In the specific case of the black hole binary GRS 1758−258, the compact object's companion is yet unknown. Several candidates are proposed but none of them is confirmed. Thus, GRS 1758−258 was monitored continually for 11 years with *RXTE*. During this time, it shows seven dim soft states that exhibit a rather peculiar track in a hardness intensity diagram. Information on the binary orbit could help to understand this behavior.

To determine the system's orbital period, we search for modulations in the X-ray light curve. This is done by applying the Fourier technique and transforming the light curve from the time to the frequency domain. Due to the uneven sampling of the light curve, the modified periodogram definition of Lomb (1976) and Scargle (1982) is used. Applying a high-pass filter to the light curve reveals a 18.475 ± 0.017 days periodicity, however, this period changes with time, first to lower, then back to higher values. Significances of the power spectral density peaks are calculated to 98.15% to 99.98% . Red and white noise, as well as filter effects as an origin to this period are excluded.

Changing with time, this signal cannot be due to an orbital modulation in the light curve. There are other systems showing superorbital periods, and at least one system has a superorbital periodicity changing with time: SMC X-1 (Clarkson et al., 2003b). For this high mass X-ray binary, an irradiation driven warp in a precessing accretion disk is proposed as the origin of the periodicity: if several warp modes compete with each other, we see a modulation in the superorbital period. However, as we do not know much about the binary system GRS 1758−258, further evidence for systems with precessing warps has to be gathered to be able compare GRS 1758−258 to a statistical relevant sample.

It is my task to convince you not to turn away because you don't understand it.

(Richard P. Feynman)

1 Snacking Stardust

"Of all the conceptions of the human mind, from unicorns to gargoyles to the hydrogen bomb, the most fantastic, perhaps, is the black hole"[1] – this is how K. S. Thorne starts the prologue to his book "Black Holes and Time Warps", and it is indeed a very true beginning. Black holes have fascinated astronomers from the very first idea until today, and still they are objects of special interest in research.

One of the first theories of black holes dates back to 1783, when John Mitchell, clergyman and amateur astronomer in England, first proposed that if light consists of particles as proposed by Newton (1730), gravity should affect it like everything else. Thus, in case of a very heavy star, gravity could be so strong as to prevent the light from escaping. However, applying Newtonian mechanics (which, as we know today, is incorrect), such a star would have had so small a radius that most astronomers considered it as mere fantasy (Carroll & Ostlie, 2007).

The concept was reconsidered in 1939 by J. Robert Oppenheimer, George Michael Volkoff and Hartland Snyder, who found the upper limit for neutron star masses (Oppenheimer & Volkoff, 1939) and described the collapse of stars that exceeded this limit and collapsed (Oppenheimer & Snyder, 1939): Black holes suddenly appeared much less fictional than before. From that time on, they were the prime objects of interest of many theoretical and experimental physicists. Detailed descriptions of stellar evolution and black hole formation can be found in any basic astronomy textbook, e.g. Carroll & Ostlie (2007).

A most extensive (but by no means complete) list of research on black holes can be found in Gallo & Marolf (2009). This section will concentrate on black hole binaries, their accretion processes and spectral states. It is in parts based on the works of Grinberg (2013) and Hanke (2011) as well as lectures of Jörn Wilms covering accretion as a topic, e.g., X-ray Astronomy I in summer term 2012.

[1] Kip S. Thorne, 1994, "Black Holes and Time Warps: Einstein's Outrageous Legacy", W. W. Norton & Co, New York/London

1.1 Accretion Disks in Black Hole Binaries: Meals on Wheels

The first question one may ask is: If photons cannot escape from a black hole, how do we observe it? This question is easily answered for black holes in binary systems where the black hole's companion is a star still burning in its core. There are ~ 20 known black hole binaries and some more promising candidates (Remillard & McClintock, 2006). This is not much, especially when compared to a supposed total number of ~ 35000 isolated black holes in our closest neighborhood (250 pc, Fender et al., 2013).

Black hole binaries, or, in general, binaries containing one compact object, can be classified according to the type of stellar companion:

- **H**igh **M**ass **X**-ray **B**inaries (HMXBs): the compact object's companion is an early type star (O- or B-type). These stars produce strong stellar winds from which matter can be accreted onto the compact object (Bondi & Hoyle, 1944). If the star is a supergiant close to filling its Roche lobe (Roche, 1849, 1850, 1851), the stellar wind can be focused onto the compact object (Friend & Castor, 1982).
- **L**ow **M**ass **X**-ray **B**inaries (LMXBs): here the compact object's companion is an evolved, late type star filling its Roche lobe. The compact object can therefore accrete matter directly from the star via the inner Lagrange point L_1 (Lagrange, 1772, see also Fig. 1.1). Due to the conservation of angular momentum, infalling

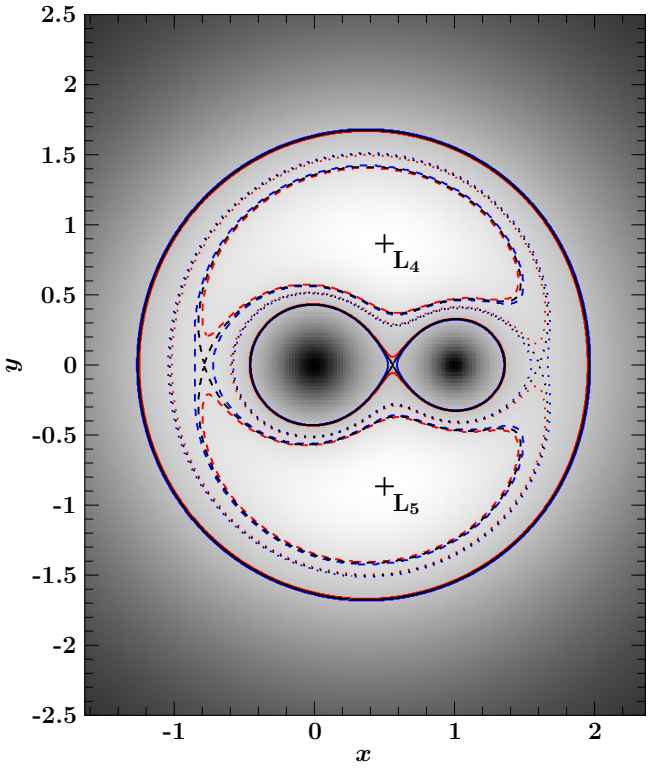

Figure 1.1: Roche potential in the x-y-plane. Brighter color indicates higher potentials. Lines show equipotential surfaces. L_1 is located at the crossing of equipotential lines between the two masses (Hanke, 2011, Fig. 1.2)

matter creates an accretion disk around the compact object (Shakura & Sunyaev, 1973). Usually, these sources are transient sources.

- Be-Binaries: the compact object's companion is a fast rotating Be-type star (B-star with emission lines), with an equatorial circumstellar gas disk. The compact object moves on an eccentric orbit, accreting matter only when close to the companions disk. For a long time, only neutron stars are observed as compact objects in these systems (see Coe, 2000, for a review), however, Casares et al. (2014) recently found a Be binary system containing a black hole.

1.1.1 Thermal Component

It is the accretion process in binary systems that betrays the black hole's hideout. Accretion is the most efficient way in physics to release large amounts of energy which is then mostly emitted in X-rays. This and the next section are based on Hanke (2011) who gave a comprehensive overview of the relevant processes.

Assuming a compact object of a mass M accreting matter in a spherically symmetric way (which is wrong as we have an accretion disk, but which is OK to get a rough estimate), there is a maximal luminosity this accretion process can produce: if the gravitational force F_g on the accreted particles of a mass m_{part} is balanced by the radiation force F_{rad},

$$\frac{GMm_{\text{part}}}{r^2} = \frac{\sigma_T S}{c} \tag{1.1}$$

with the Thomson cross section σ_T and the energy flux

$$S = \frac{L}{4\pi r^2} \tag{1.2}$$

containing the luminosity L, the accretion flow as a source of energy is cut off. The corresponding luminosity is called the Eddington luminosity

$$L_{\text{Edd}} = \frac{4\pi GMm_{\text{part}}c}{\sigma_T} \sim 1.3 \cdot 10^{38}\,\text{erg}\,\text{s}^{-1} \cdot \frac{M}{M_\odot}. \tag{1.3}$$

Thus, in this simplified model, accretion is only possible as long as the luminosity is below the Eddington luminosity.

As long as accretion goes on, the released energy can be estimated for a mass m accreted from infinity to a stable circular orbit at radius r:

$$E_{\text{rel}} = E(\infty) - E(r) = \frac{1}{2}\frac{GmM}{r} \tag{1.4}$$

Accreted to the Schwarzschild radius of a black hole, i.e., the radius where the escape velocity equals the speed of light, $r_S = 2GM/c^2$, the released energy would thus be

$$E_{\text{rel}} = \frac{1}{4}mc^2. \tag{1.5}$$

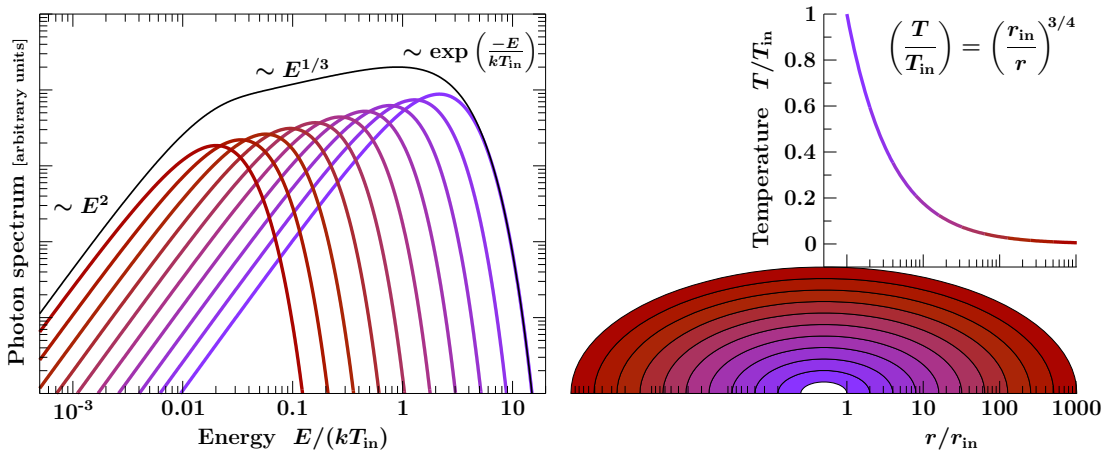

Figure 1.2: Composite spectrum and temperature profile of an optically thick accretion disk (Hanke, 2011, Fig. 1.6)

This released energy is converted to random thermal motion by the viscosity of the accretion disk. Note that the molecular viscosity as we know it proves too small to affect astrophysical disks. The actual process taking place is yet poorly understood. Theories involve, e.g., magnetohydrodynamical instabilities amplifying magnetic field inhomogeneities in the accretion disk (Balbus & Hawley, 1991).

The viscosity of the disk is needed to exert torques as the accreted matter has to lose its angular momentum when moving inward (Shakura & Sunyaev, 1973; Frank et al., 2002). If we define the amount of mass crossing radius R in the accretion disk

$$\dot{M} = -2\pi R \cdot \Sigma \cdot v_{\rm R} \tag{1.6}$$

with the surface density of the disk Σ and the radial velocity $v_{\rm R}$ of the accreted particles, and consider that at the radius of the inner edge of the disk $R_{\rm in}$, there has to be no torque, we can calculate the viscous dissipation rate per unit area to

$$D(R) = \frac{{\rm d}E}{{\rm d}A{\rm d}t} = \frac{3GM\dot{M}}{4\pi R^3}\left[1 - \left(\frac{R_{\rm in}}{R}\right)^{1/2}\right]. \tag{1.7}$$

In an optically thick medium, the dissipated energy in a two sided disk is thermalized according to the Stefan-Boltzmann-Law

$$2\sigma_{\rm SB} T^4 = D(R) \tag{1.8}$$

and the temperature profile is therefore

$$T(R) = \left\{\frac{3GM\dot{M}}{8\pi R^3 \sigma_{\rm SB}}\left[1 - \left(\frac{R_{\rm in}}{R}\right)^{1/2}\right]\right\}^{1/4}. \tag{1.9}$$

Thus we know the radial dependence of the temperature

$$T(R) \propto R^{-3/4} \tag{1.10}$$

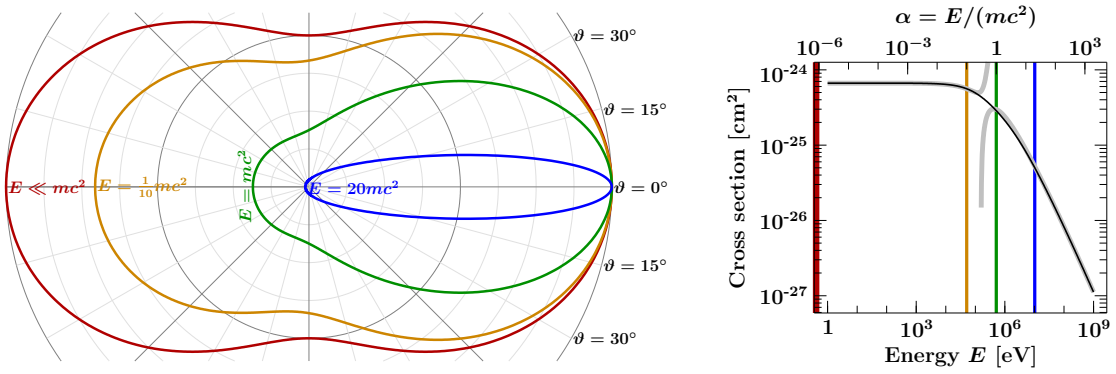

Figure 1.3: Angular dependence of scattering probability (left) and total Klein-Nishima cross section (right) for Compton scattering (Hanke, 2011, Fig. 1.8)

As in an optical thick medium, radiation is emitted as blackbody radiation

$$T_{\mathrm{bb}} = \left(\frac{L}{4\pi R^2 \sigma_{\mathrm{SB}}} \right)^{1/4} \tag{1.11}$$

we can integrate over all radii $R_{\mathrm{in}} \leq r \leq R_{\mathrm{out}}$ and get a composite spectrum (Fig. 1.2 with a Rayleigh-Jeans tail at low and a Wien tail at high energies and a slope $\propto E^{1/3}$ in between (Lynden-Bell, 1969).

1.1.2 Comptonization and Reflection

Up to now we only considered the thermal radiation component caused by the accretion disk directly. However, this is only one part of the final spectrum we observe from black holes. We have not yet considered direct interaction between the photons and particles (mainly electrons), taking place in from of Compton scattering (Compton, 1923)

$$\lambda - \lambda' = \frac{h}{m_{\mathrm{e}} c}(1 - \cos\theta) \tag{1.12}$$

or

$$\frac{E'}{E} = \frac{1}{1 + \frac{E}{m_{\mathrm{e}}c^2}(1 - \cos\theta)}, \tag{1.13}$$

the new wavelength dictated by the scattering angle θ. The cross section for this process was calculated by Klein & Nishina (1929) and is illustrated in Fig. 1.3.

In the case of a hot electron plasma with a temperature T_{e}, photons may thus gain energy, referred to as inverse Compton scattering (see e.g. Rybicki & Lightman, 1979; Zdziarski, 1985; Lightman & Zdziarski, 1987, and references therein)

$$\frac{E'}{E} \sim 1 + \frac{4kT_{\mathrm{e}} - E}{m_{\mathrm{e}}c^2} \tag{1.14}$$

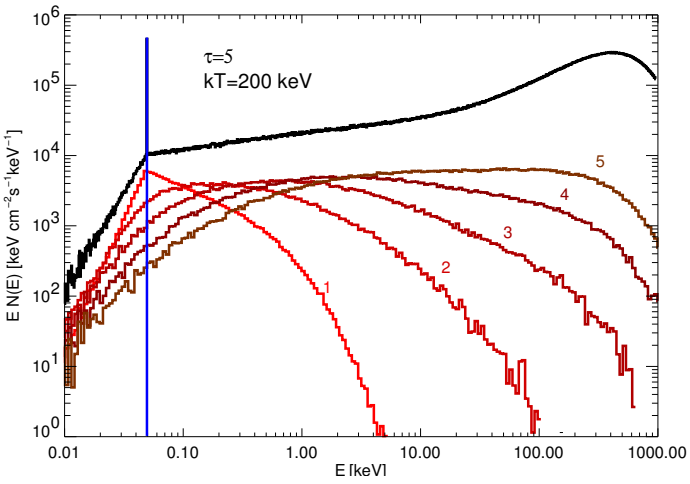

Figure 1.4: Simulated spectra from inverse Compton scattering of photons ($E = 500\,\mathrm{eV}$) and electrons ($kT_\mathrm{e} = 200\,\mathrm{keV}$) in a region with an optical depth τ for different numbers of scattering processes (Wilms, lecture "X-ray Astronomy I")

As most photons scatter quite often before they leave the scattering region and are observed, the spectral changes by can be significant (Fig. 1.4).

The exact origin of the Comptonized spectrum (e.g., Titarchuk, 1994) is yet unclear, two possible models are discussed:

- Sandwich corona model / sphere and disk model: The Comptonization is caused by a hot electron plasma surrounding the disk (e.g., Haardt & Maraschi, 1991; Dove et al., 1998).
- Lamppost model: The Comptonization comes from the base of a jet (e.g., Matt et al., 1992; Markoff et al., 2005; Miniutti et al., 2007).

Nowak et al. (2011) summarize the different possible accretion geometries (Fig. 1.5): Soft photons emitted by the possibly truncated disk are Compton-upscattered in a spherical or toroidal corona around the disk, or at the jet base, leading to a powerlaw continuum. The jet itself can also produce synchrotron radiation and photons can be upscattered by the same particles they are emitted from. This mechanism is called synchrotron

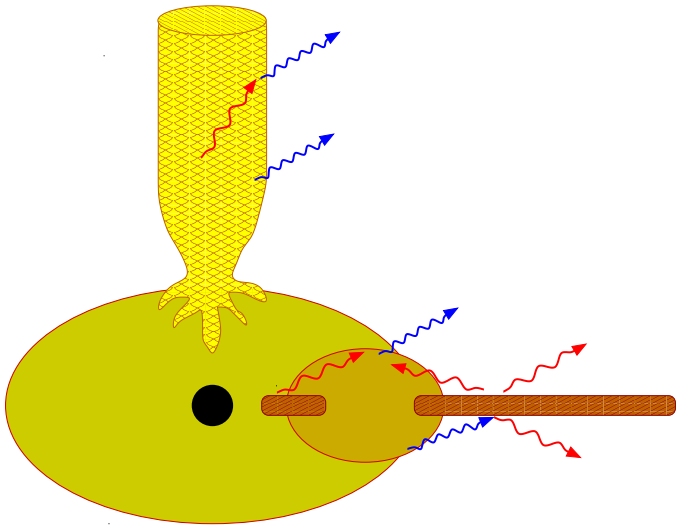

Figure 1.5: Illustration of different accretion geometries: Soft photons (red) are emitted by the disk (brown) and upscattered in a corona region (dark yellow) or at the base of a jet (yellow) (Nowak et al., 2011, Fig. 1.9).

self-Compton effect. When higher energetic power law photons hit the disk, they are again reprocessed via Compton scattering (leading to a Compton reflection hump, see, e.g., Lightman & White, 1988; Magdziarz & Zdziarski, 1995) or fluorescent line emission.

1.2 Spectral States: Black Holes' Digestion

The previous section talked about the different contributions to a black hole's total spectrum. What was not yet considered is the amount that each of them contributes, and as we might expect, this amount is by no means constant with time. In fact, black holes show variability on all time scales (Fig. 1.6).

Typically, we divide the states into two main X-ray states first discovered for the black hole binary Cyg X-1 by Tananbaum et al. (1972):

- Soft/high state: the spectrum is dominated by the thermal soft X-rays of the accretion disk. There is little to no variability in the light curve.
- Hard/low state: the powerlaw component in the hard X-rays dominates the spectrum. The light curve may show a high variability.

Fig. 1.7 shows the different states using the example of LMC X-3 and Cyg X-1.

Fender et al. (2004) and Remillard (2005) proposed a method to classify black hole spectral states using the hardness intensity diagram (HID, see also Fender et al., 2009; Motta et al., 2009; Belloni, 2010; Corbel et al., 2013, and references therein). This diagram relates the spectral hardness, i.e., the ratio of high to low energy flux or count rate

$$H = \frac{F_{\text{hard}}}{F_{\text{soft}}}, \tag{1.15}$$

to the brightness of the source (total flux or count rate). Using this, we have of course to keep in mind that spectral hardness is not a very distinct dimension. Lower hardness can be due to either an increase in the flux of the black body disk component or a steepening

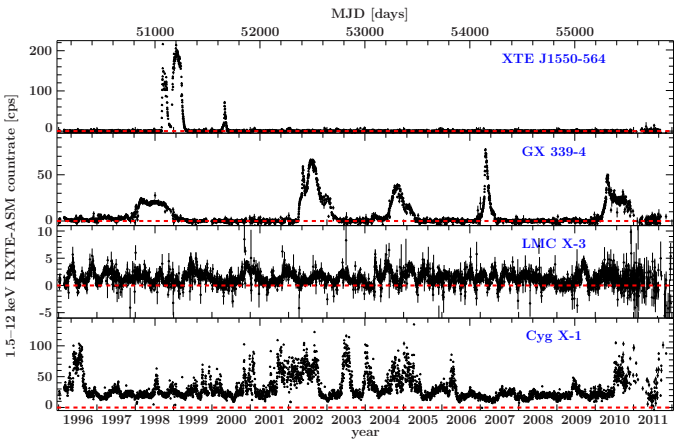

Figure 1.6: Black hole variability on all time scales: Whereas some sources are invisible save for a few single outbursts, others show regular flares and some exhibit a constant flickering at different amplitudes (Grinberg, priv. comm.)

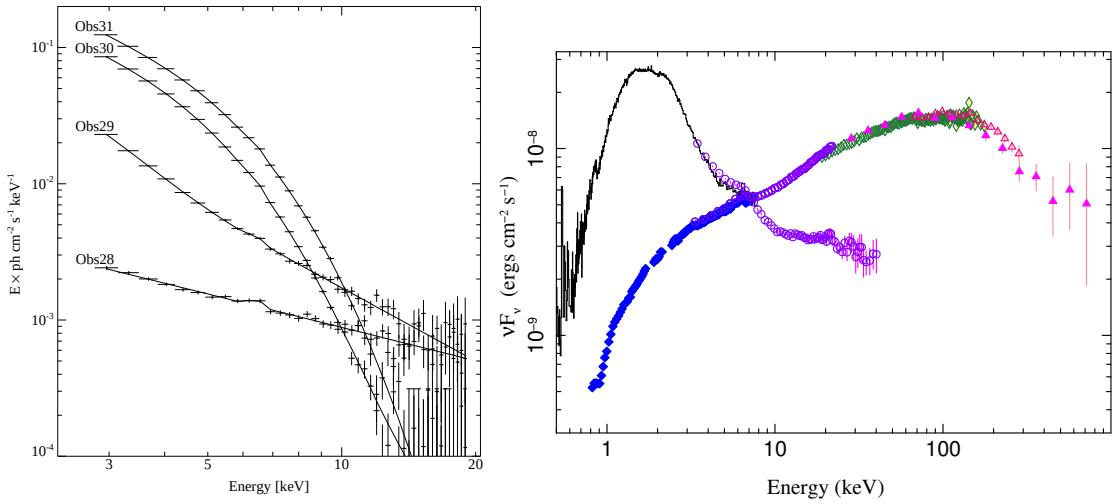

Figure 1.7: *Left:* Hard and soft state of LMC X-3 (Wilms et al., 2001, Fig. 4); *right:* Hard and soft states of Cyg X-1 (Wilms, lecture "X-ray Astronomy I").

of the powerlaw or a combination of both. However, most transient sources show a surprisingly similar behavior in an HID (Fig. 1.8, central panel).

- Starting from quiescence, they become brighter at about the same high hardness. Radio emission can be observed. The source is now in the hard state.
- At some point, the source stops to brighten and the spectrum becomes softer. The source enters the hard intermediate state.
- While softening, the source sometimes shows radio flares. It approaches the soft intermediate state. At a certain point called jet line, the jet is supposed to switch off, radio emission drops to (near) nonexistence.
- Once the source arrives in the soft state, it starts dimming again. In this process, the softness varies much more than the hardness does at increasing brightness.
- Before the source dims back into quiescence, the brightness decrease pauses and the spectrum hardens again. The source then continues dimming and completes the hysteresis in its HID.

In practice, each source of course shows some individualities, varying more or less in brightness or hardness, but in general, all observations seem to be compatible with this picture.

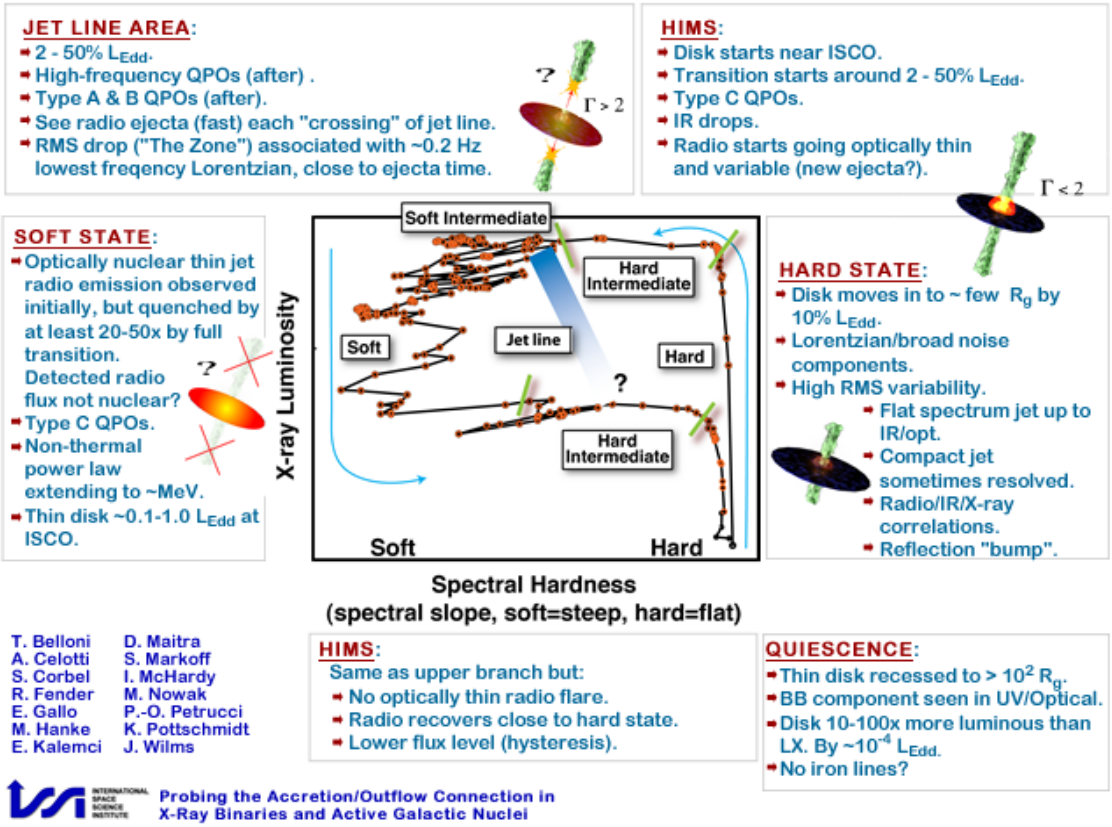

Figure 1.8: Image from http://www.sternwarte.uni-erlangen.de/proaccretion/

In the matter of physics, the first lessons should contain nothing but what is experimental and interesting to see. A pretty experiment is in itself often more valuable than twenty formulae extracted from our minds.

(Albert Einstein)

2 Overview of Observations

Already in my Bachelor thesis (Obst, 2011), I was able to investigate one of the most fascinating objects in Physics, a microquasar. I was able to continue the analysis of my previous dataset and carry it into a new field of astronomy: Time series analysis.

The first chapter gives a short introduction to the satellite used to collect the data, *RXTE*, and to the microquasar GRS 1758−258 itself, including the previous results this work is based on.

2.1 *RXTE*

The Rossi X-ray Timing Experiment (*RXTE*), a NASA mission launched in 1995 into a Low Earth Orbit with an altitude of about 600 km (Bradt et al., 1993), carried three X-ray detectors: The All-Sky Monitor (ASM) (Levine et al., 1996) consisted of three wide-angle cameras with proportional counters monitoring the sky for sources that show an unusual behavior. The High Energy X-Ray Timing Experiment (HEXTE; Rothschild et al., 1998), consisted of 2×4 NaI/CsI phoswich scintillation detectors, mainly gathered timing information for compact objects and Active Galactic Nuclei (AGN).

This work uses data taken by the third instrument on *RXTE*, the Proportional Counter Array (PCA; Jahoda et al., 1996, 2006; Zhang et al., 1993). The array consisted of five (originally) identical Proportional Counter Units (PCUs). Each of them had a geometrical detection area of $\sim 1600\,\mathrm{cm}^2$. If an X-ray photon wanted to be detected by one of the PCUs, it first had to pass a mechanical collimator (see Fig. 2.1), a grid of hexagonal tubes of beryllium copper mounted exactly perpendicular to the underlying detector surface. The Field of View (FoV) of the collimator had a full width at half maximum (FWHM) of about 1°. The larger the angle between the travelling direction of the photon and the pointing direction of the PCA, the smaller was the probability that the photon would actually reach the detector (see Fig. 2.1) and not be reflected or absorbed by the collimator material. After the collimator, the photon would pass an aluminum coated Mylar window

covering the first volume of the proportional counter.

A proportional counter consists of a chamber filled with an inert gas. An infalling photon or particle of high energy will deposit its energy in the chamber by ionizing the gas molecules. The number of ion pairs produced by the infalling photon or particle is proportional to its energy. An electric field in the chamber accelerates the ion pairs toward cathode and anode. In this process, the electrons will gain more energy as their mass is much smaller than the one of the ions. Shortly before reaching the anode wire where the electric field is highest, each electron will therefore produce an ionization avalanche which is then detected by the anode. A quench gas mixed to the inert gas makes sure that there is no additional avalanche started e.g. if the discharging ions acquire their electrons on higher energy levels and then decay by emitting a photon. Thus, the dead time of the detector is limited. For details on proportional counters, see e.g. Grupen & Shwartz (2008).

In the case of the PCUs, a multi-wire proportional counter was used (Jahoda et al., 1996, 2006; Zhang et al., 1993): the first volume contained 20 anodes separated by aluminum wall cathodes which supported the second Mylar window. It was filled with propane and used as a veto layer for electrons and as a front anti-coincidence shield. Behind the second Mylar window lay the main counter filled with xenon and 10% methane as

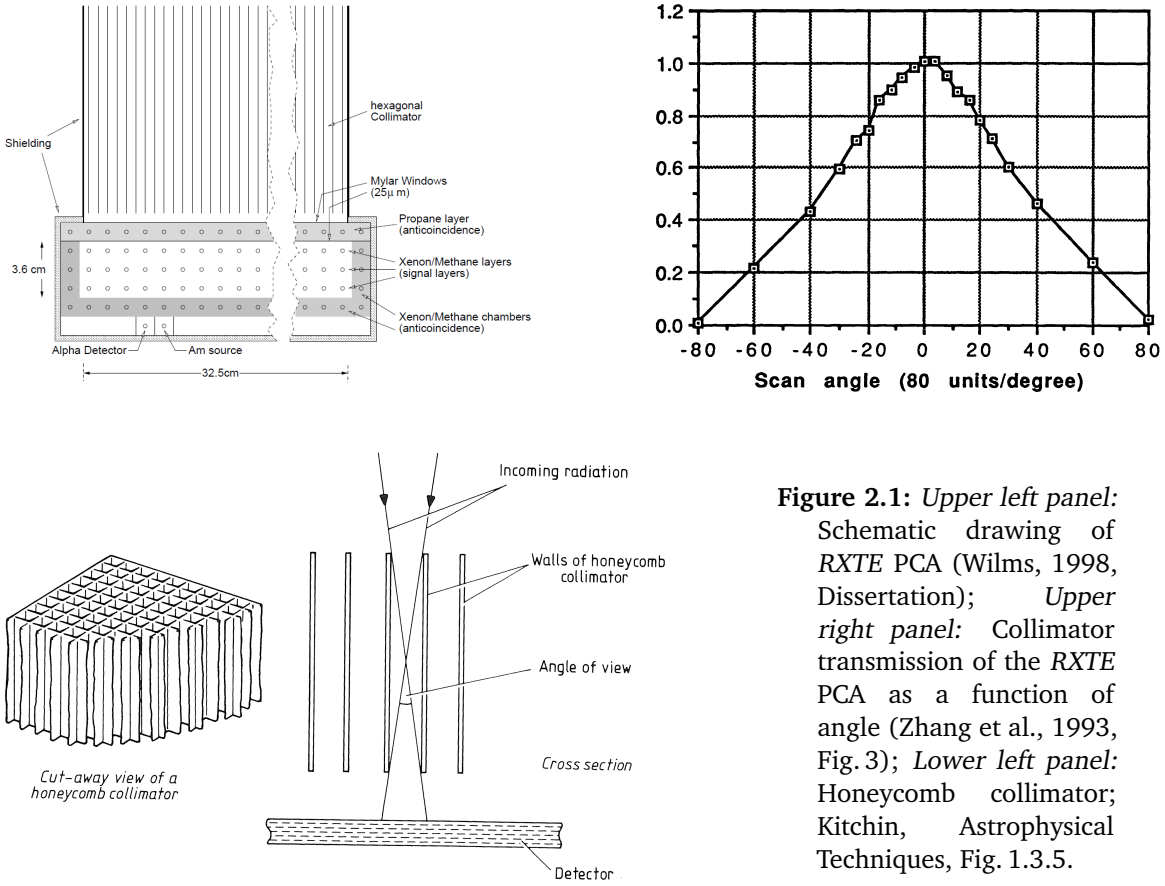

Figure 2.1: *Upper left panel:* Schematic drawing of *RXTE* PCA (Wilms, 1998, Dissertation); *Upper right panel:* Collimator transmission of the *RXTE* PCA as a function of angle (Zhang et al., 1993, Fig. 3); *Lower left panel:* Honeycomb collimator; Kitchin, Astrophysical Techniques, Fig. 1.3.5.

a quench gas, consisting of three layers with 20 anodes each. The cells were divided by wire walls, alternate cells were connected to either the left or the right amplifier chain. Thus the detector was basically divided in halves, which was significant for data screening and background modeling. The response matrices for the two halves were identical. For normal observational data analysis, both halves were combined. The back layer was used as second coincidence shield and xenon veto layer. These layers identified and tagged photons that came of an off-source direction as well as calibration events. Below the main counter there was an ^{241}Am source used for energy calibration: ^{241}Am decays with a half-life of 432.2 years to ^{237}Np by an α-decay

$$^{241}_{95}\mathrm{Am} \longrightarrow ^{237}_{93}\mathrm{Np} + ^{4}_{2}\mathrm{He} + \gamma. \tag{2.1}$$

Thus, if an α-particle and a photon were measured at the same time, the photon was most probably emitted in this decay and therefore has a known energy of 59.6 keV, and the event was tagged as calibration event by the coincidence shield. The detector body was constructed of aluminum and surrounded by a graded shield of tin and tantalum.

RXTE was switched off in January 2012 after a lifetime of more than 16 years. Thus, it is not surprising that the PCA experienced some problems in the course of its life: The first of the PCUs (PCU0) lost its propane layer after 5 years, the second (PCU1) another 6 years later, due to a micrometeorite. Both PCUs were working until the end, but with a different gain and higher background. There are several calibration epochs between which the high voltage was changed. In the final years, only two of the PCUs were working at the same time, to save energy and extend the lifetime of the PCA. To avoid problems connected to calibration, only data from the best calibrated PCU (PCU2) were used throughout this work.

2.2 Monitoring of GRS 1758−258

The black hole candidate GRS 1758−258 (see Chapter 1 for an introduction to black hole binaries) was monitored by *RXTE* periodically between 1997 and 2008. The spectral analysis of the extensive dataset has already been done (Obst, 2011), a short introduction to microquasars as well as detailed comments on the analysis can be found there. As the timing analysis of the data is based on the spectral results, this section summarizes the relevant parts of the previous work (see there for detailed spectral parameters and interpretation). This work will shortly be submitted for publication to A&A where "we" is the pronoun commonly used. Thus, it would be highly inconsistent to do otherwise here. The reader is welcome to see it as "you and I"!

GRS 1758−258 is a black hole binary discovered in 1990 during observations of the Galactic Center region (Fig. 2.2, also see Heindl & Smith, 2002, for the exact location) by the *Granat* satellite (Mandrou, 1990; Syunyaev et al., 1991). As one of only three known persistent, mostly hard state black hole binaries in our Galaxy (GRS 1758−258, 1E 1740.7−2942 and Cyg X-1[1]), GRS 1758−258 has since been observed in various en-

[1] Note that Cyg X-1 has been in the soft state for more than two years now (Grinberg et al., 2013)

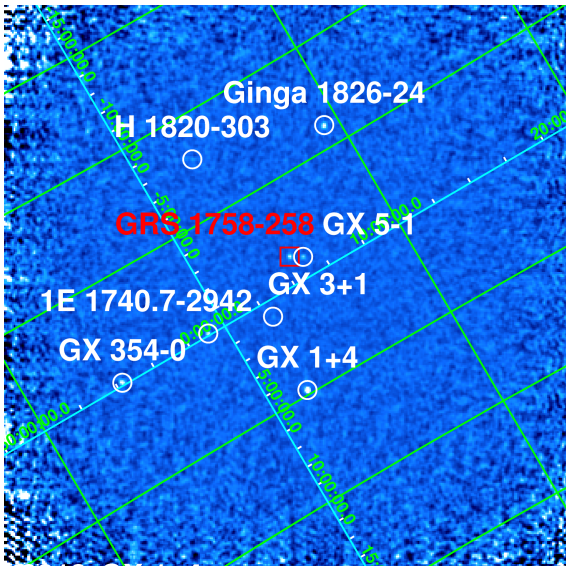

Figure 2.2: *INTEGRAL*-ISGRI count rate mosaic image in the 20–40 keV band obtained during Galactic Center Region Key Programme observations performed in spring 2007. (Lohfink, priv. comm.)

ergy ranges (e.g., Rodriguez et al., 1992; Cadolle Bel et al., 2006; Pottschmidt et al., 2008; Muñoz-Arjonilla et al., 2010; Soria et al., 2011, and references therein). As radio observations showed a double-lobed counterpart (Rodriguez et al., 1992; Hardcastle, 2005), GRS 1758−258 is considered a microquasar.

Pottschmidt et al. (2008) were able to describe broad band spectra of GRS 1758−258 taken by the *RXTE* and *INTEGRAL* satellites with an absorbed powerlaw cut off at high energies, a black body disk component in the soft X-rays and a weak neutral iron Kα line (Fig. 2.4). Their spectra are averaged over epochs of about 3 months and, although GRS 1758−258 is not a transient X-ray source like most of the known microquasars, it still displays different spectral states, a behavior typical for transient sources (Pottschmidt

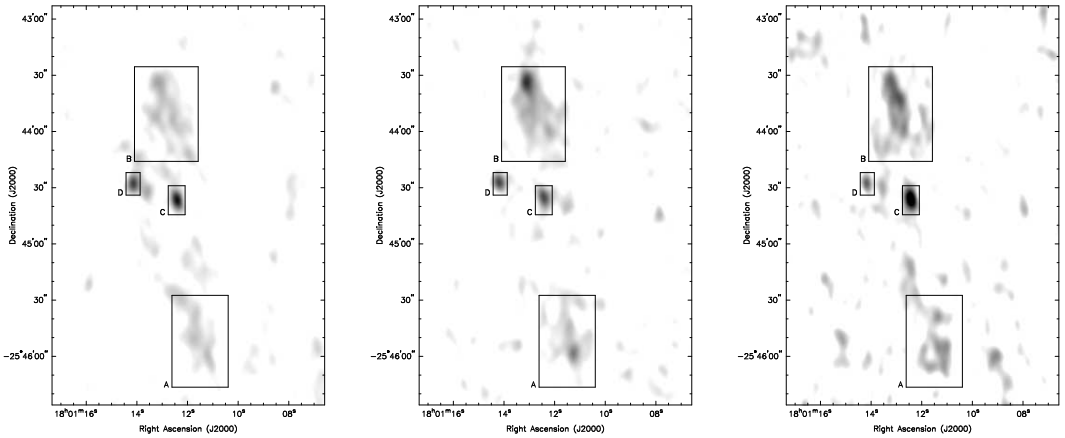

Figure 2.3: Radio lobes of GRS 1758−258 at three frequencies: 1.4 GHz (left), 4.9 GHz (center) and 8.4 GHz (right) with a resolution of 9.2 × 5.8 arcsec taken with the NRAO Very Large Array (VLA) (Hardcastle, 2005, Fig. 1)

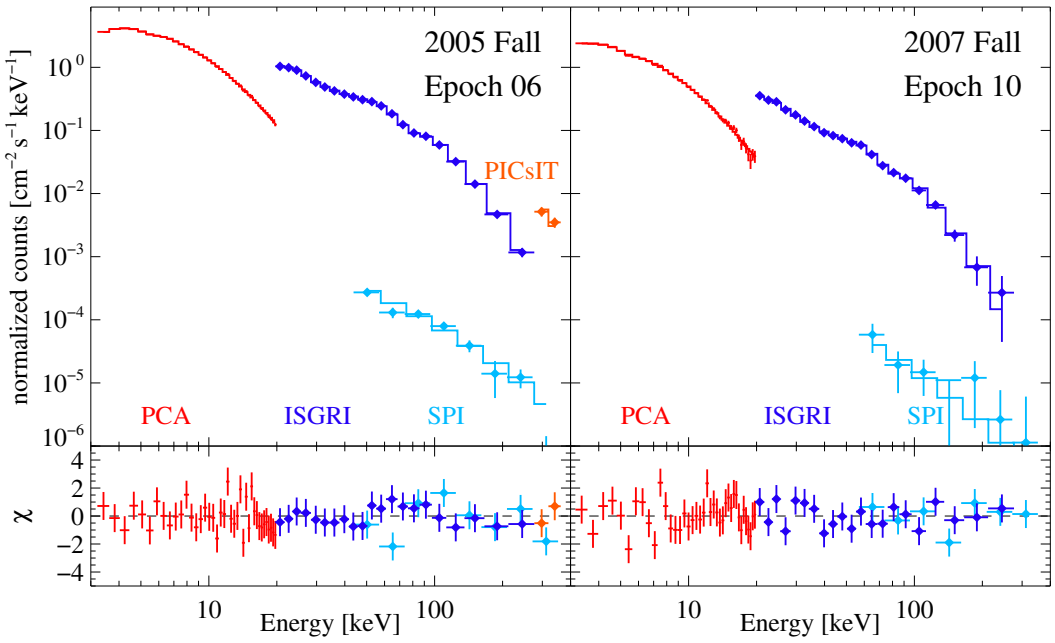

Figure 2.4: Broadband spectra of GRS 1758−258 (Pottschmidt et al., 2008, Fig. 3)

et al., 2008), making more detailed observations necessary for further information. Usually GRS 1758−258 is found in the hard state. The soft state, however, is peculiar: GRS 1758−258 dims significantly while the spectrum is softening. Pottschmidt et al. (2008) suggested a "p"- rather than a "q"-shaped track in the hardness intensity diagram (HID, see 1.2). However, looking at the complete data available now, we conclude that GRS 1758−258 as a persistent source just skips the quiescent state and only moves on the upper part of the usual "q" in its HID (Obst, 2011). There, taking a short cut from the hard (intermediate) directly to the soft state, it shows a clear hysteresis in state transitions (Fig. 2.5).

GRS 1758−258 has been observed by the *RXTE* PCU in 1.0–1.5 ks long pointed snapshots (Smith et al., 2001, 2002). These snapshot observations were done in monthly intervals in 1996, weekly through 2000, and twice a week from 2001 March to 2007 October. Each year there is a gap from November to January as the Sun was too close to the Galactic Center, i.e., the pointing direction to GRS 1758−258 (Obst, 2011).

Because of its location only 0.°66 away from the very bright X-ray binary GX 5−1 (Fig. 2.2, GRS 1758−258 is a difficult source to observe with *RXTE*. The monitoring could therefore only be realized using offset pointings away from GX 5−1 (Smith et al., 2001, 2002), i.e., using the triangular response of PCA's collimator to reduce the influence of GX 5−1 further. Response matrices were built such that they take the effect of the offset pointings into account (Obst, 2011).

As GRS 1758−258 is faint and located in the Galactic Plane, close to the Galactic Center, RXTE spectra of the source also contain a strong background component caused by the Galactic Ridge emission. To distinguish between source counts and Galactic Ridge

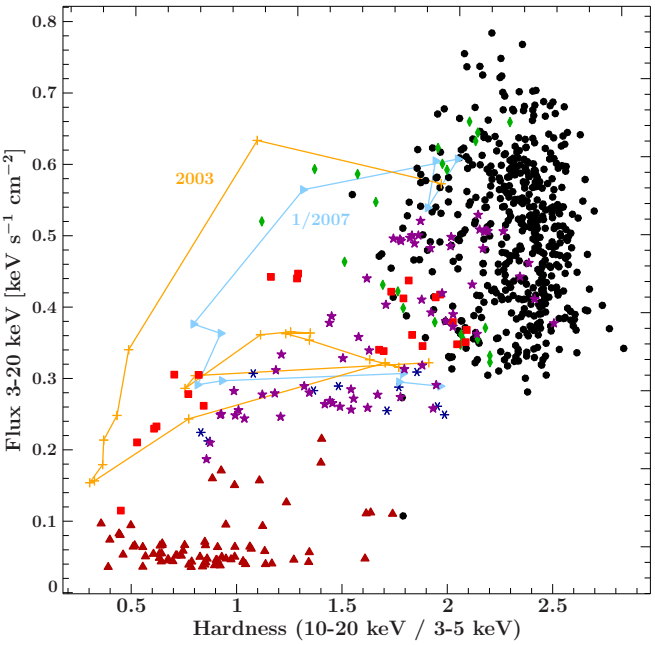

Figure 2.5: Hardness intensity diagram (HID) from *RXTE* monitoring observations of GRS 1758−258 from 1997 until 2007. Seven dim soft states are highlighted as in Fig. 2.7. To show the "q"-shaped track of GRS 1758−258 in the HID, the data points of two soft state passages (2003 and 1/2007) are connected (Obst, 2011, Fig. 3.2a)

counts, background observations totaling 13 ks, 1.°5 offset from GRS 1758−258, were performed by *RXTE* in 1999. All spectral analysis was done using the *Interactive Spectral Interpretation System* (ISIS; Houck & Denicola, 2000; Houck, 2002; Noble & Nowak, 2008). We were able to model the local Galactic Ridge emission with two bremsstrahlung components and an iron line complex (Obst, 2011) according to high resolution *Suzaku* observations of the Galactic Ridge (Ebisawa et al., 2007). We assume that there is no local variation of the Galactic Ridge emission, and then added this model with all parameters fixed to the spectral model of GRS 1758−258 (Obst, 2011). See Fig. 2.6, left, for

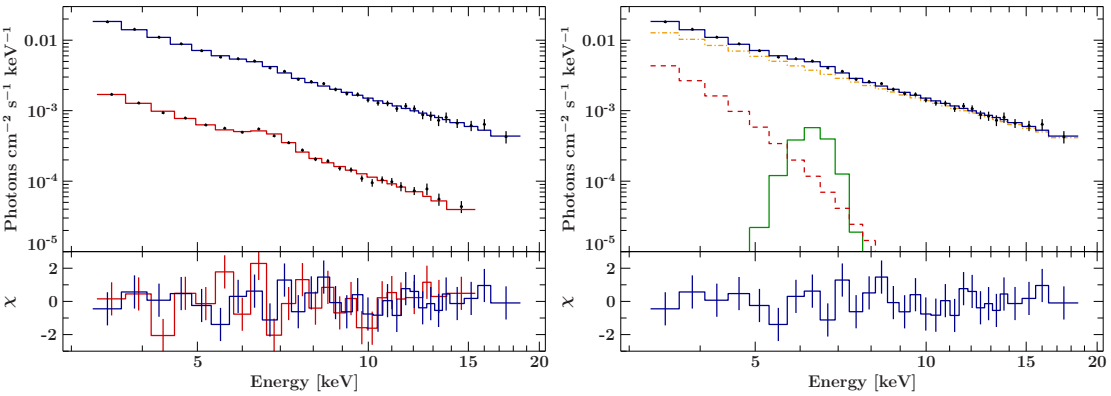

Figure 2.6: *Left:* Spectrum for the 2007 July 23 observation of GRS 1758−258 from the source position, i.e., including the source contribution and the Galactic Ridge emission (blue), and spectrum for the Galactic ridge emission alone (red). *Right:* example of an instrument background subtracted spectrum taken by *RXTE* on 2007 July 23, containing the absorbed power-law component (dash-dotted line), the disk (dashed line), and the iron line (green solid line). For clarity the constant Galactic Ridge model part is not shown.

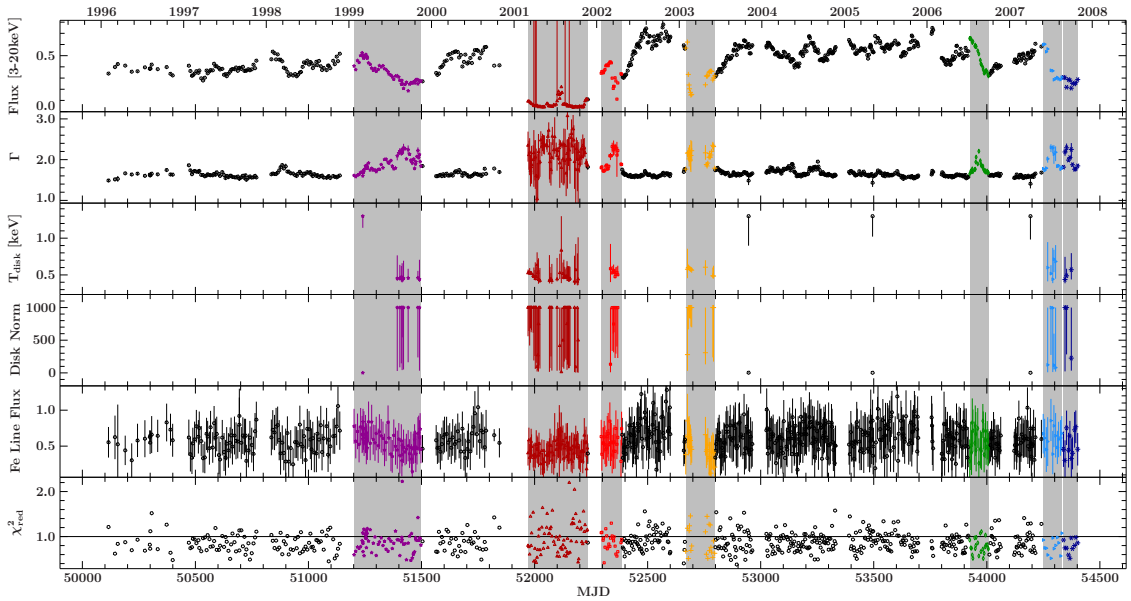

Figure 2.7: Spectral parameters from *RXTE* monitoring observations of GRS1758−258: flux in $\mathrm{keV\,s^{-1}\,cm^{-2}}$ in the 3–20 keV band, fitted to the spectra, photon index, temperature, and normalization of the disk component, total flux of the additional iron line in $10^{-3}\,\mathrm{ph\,s^{-1}\,cm^{-2}}$ and the reduced χ^2. Soft states are highlighted for episodes reaching a photon index softer than 2. The Figure is based on Obst (2011, Fig. 2.7).

the amount of the Galactic Ridge emission in the GRS 1758−258 data, as well as (Obst, 2011) for the Galactic Ridge spectral parameters.

All spectra were then modeled using an empirical model consisting of an absorbed powerlaw (`phabs × powerlaw`) and an additional iron line (`egauss`) (Obst, 2011). As Soria et al. (2011) do not report an iron line for their *XMM* analysis, we simulated *XMM* spectra based on some of our best fit models: A relatively broad iron line ($\sigma \sim 800$ eV) as seen in our fits appears to be so smeared in a highly resolved *XMM* spectrum that for *XMM* it is not required in the model. Some softer spectra also require an additional black body disk (`diskbb`) for improving the fit. For each spectrum, the source flux (i.e., not containing the Galactic Ridge background) was calculated from the best fit spectra (Obst, 2011). As shown in Fig. 2.7, flux and powerlaw photon index show a clear anti-correlation with a Spearman rank coefficient of 0.46: with increasing photon index the flux decreases, i.e., the spectrum of GRS 1758−258 dims and softens. We classified as soft state all data from where GRS 1758−258 starts softening up to photon indices softer than 2, to where it is back in the hard state (Obst, 2011). Between 1997 and 2008, we found 7 dim soft states (highlighted in Fig. 2.7). During the 2001 soft state, the source almost turned off completely. The blackbody disk emission appears only during these soft states where the low flux increases the uncertainties of the best fit parameters (Obst, 2011).

The roots of education are bitter, but the fruit is sweet.

(Aristotle)

3 Timing Techniques

For studying X-ray binaries, it is important to find the companion star of the compact object. The orbital parameters of a binary system play a major role in the production of the X-rays observed by mankind. Stellar type and distance of the companion influence the accretion mechanism of the compact object and thus the spectrum emitted in this process as well as the short and long-term variations in the X-ray light curve: In the case of a low mass companion, accretion via Roche lobe overflow might cause a hot spot on the accretion disk. Many such systems are transient sources, being in quiescence most of the time while the accretion disk is filling, and going into outburst once the disk becomes too massive. If the donor star is massive and produces a strong, maybe clumpy stellar wind, many absorption lines can be seen in the X-ray spectrum (Sako et al., 1999; Fürst et al., 2011; Kühnel, 2011; Oskinova et al., 2013; Sundqvist & Owocki, 2013, and references therein). If the compact object is an X-ray pulsar, a correction for the binary orbit has to be applied to the light curve in order to find its pulse period.

The usual way to find out about the orbital parameters is looking at the light curve: The binary orbit causes a slight, periodic modulation on the light curves of each of the two objects. Timing analysis of the 11 years *RXTE* monitoring light curve therefore is a promising ansatz.

There are various methods to determine periodicities in a dataset in general. This chapter shortly describes the easiest way, epoch folding, as well as the more difficult Fourier techniques.

3.1 Epoch Folding

The easiest method to test a dataset for periodicities is epoch folding (Leahy et al., 1983b; Schwarzenberg-Czerny, 1989). A detailed description can be found in Kühnel (2011), this section contains a short summary: For a certain set of test periods p_{test}, the light

curve of length L is folded to the period length:

$$\rho(t) = \sum_{n-0}^{N-1} F(t + np_{\text{test}}) \otimes R(t) \tag{3.1}$$

with $N = L/p_{\text{test}}$ and the rectangular function

$$R(t) = \begin{cases} 1, & \text{for } 0 \leq t \leq T, \\ 0, & \text{otherwise.} \end{cases} \tag{3.2}$$

This results in a "pulse profile" ρ. If the periodicity p in the dataset is different from p_{test}, the pulse profile is relatively flat as the peaks and dips are averaged out. If $p = p_{\text{test}}$, the pulse profile shows a distinct variation with phase. Doing this for many test periods and comparing the resulting pulse profiles against a constant using a χ^2- or z^2-test, the correct periodicity can be found, even if the pulse shape is not sinusoidal.

While gaps in the dataset do not affect the results, however, this method cannot be applied to very short or coarsely sampled light curves: A minimum length of about $\mathrm{d}t \geq 20 \times p$ is necessary to obtain reasonable results when folding the light curve, as well as a binning better than $t_{\text{res}} \leq p/10$. With a mean sampling of $t_{\text{res}} \sim 14\,\text{days}$ of the GRS 1758−258 light curve, we could thus look for periods above $p \sim 140$ days, corresponding to a very wide binary system. As we cannot assume this to be the case for GRS 1758−258, epoch folding is not applicable for our dataset.

3.2 (Fast) Fourier Transform

In cases where epoch folding cannot be used, the Fourier technique is applied. This summary of the Fourier method is based on the more detailed works of van der Klis (1989), Pottschmidt (2002) and Grinberg (2013). We will closely follow van der Klis (1989) in the remaining section.

The (continuous or discrete) Fourier transform (Fourier, 1822) allows to transform signals from the time (or spatial) domain into the frequency domain: It decomposes a signal into sine waves. An infinitely extended continuous function $x(t)$ is transformed to

$$a(\nu) = \int_{-\infty}^{+\infty} x(t) \mathrm{e}^{-2\pi\nu \mathrm{i} t} \mathrm{d}t \tag{3.3}$$

and the other way round,

$$x(t) = \int_{-\infty}^{+\infty} a(\nu) \mathrm{e}^{2\pi\nu \mathrm{i} t} \mathrm{d}\nu \tag{3.4}$$

where $\mathrm{i}^2 = -1$.

For many cases this transform can be calculated analytically. For example, transforming a sine wave returns a delta function at the respective frequency. Thus, theoretical predictions concerning the shape of a Fourier transform are usually based on the continuous transform.

However, what we usually deal with in astronomy are time series of fluxes x_k: For a time bin k a flux x has been observed in a certain energy band. We therefore use the discrete Fourier transform to get from an equally spaced time series of length N to a series of N equidistant frequencies. Equations 3.3 and 3.4 then look the following:

$$a_j = \sum_{k=0}^{N-1} x_k e^{-2\pi\nu_j i t_k} \qquad j = -\frac{N}{2}, \ldots, \frac{N}{2} - 1 \tag{3.5}$$

or

$$x_k = \frac{1}{N} \sum_{j=-N/2}^{N/2-1} a_j e^{2\pi\nu_j i t_k} \qquad k = 0, \ldots, N-1 \tag{3.6}$$

For uncorrelated flux values x_l the frequency values a_j are also uncorrelated. A complete description of the discrete signal is obtained. One may now be puzzled about the imaginary component of the a_j, but on the second look, we see that positive as well as negative frequencies are considered. This makes the imaginary components cancel out, and we get a real number as a final result. In practice, the real component of the a_j describes the amplitude of the respective sinusoid, whereas the imaginary component denotes the phase.

However, with a discrete time series we are not able to observe any frequency we want to: there is an upper limit at half the sampling frequency:

$$\nu_{N/2} = \frac{1}{2}\frac{N}{T} \tag{3.7}$$

where T denotes the total length of the time series. This frequency is called Nyquist frequency (Nyquist, 1928; Shannon, 1949).

There are algorithms that allow to efficiently compute a discrete Fourier transform: the Fast Fourier Transform (FFT, Cooley & Tukey, 1965). This method dates back as early as Carl Friedrich Gauss who used it around 1806. His work was not published in his lifetime but only about thirty years after his death (Gauss, 1866; Press et al., 1992). The first official publication was by Runge (1903) and Runge (1905). By reusing intermediate results, the operation time to compute a discrete Fourier transform can be reduced from $\mathcal{O}(N^2)$ to $\mathcal{O}(N \log N)$ which results in a significantly faster calculation especially for large N.

3.3 The Power Spectrum

According to Parseval's theorem (Parseval des Chênes, 1806), the total power in a signal stays the same whether we compute it in the time (or space) or frequency domain:

$$\sum_{k=0}^{N-1} |x_k|^2 = \frac{1}{N} \sum_{j=-N/2}^{N/2-1} |a_j|^2 \tag{3.8}$$

This can be applied to the total variance of the dataset:

$$\mathrm{Var}(x_k) = \sum_k (x_k - \bar{x})^2 = \sum_k x_k^2 - \frac{1}{N}\left(\sum_k x_k\right)^2 \tag{3.9}$$

$$= \frac{1}{N}\sum_j |a_j|^2 - \frac{1}{N}a_0^2 = \frac{1}{N} = \sum_{\substack{j=-N/2,\\ j\neq 0}}^{N/2-1} |a_j|^2 \tag{3.10}$$

Now the power spectrum, giving the fraction of the total light curve variance at the respective frequency, can be defined as

$$P_j = \frac{2}{N_{\mathrm{Ph}}}|a_j|^2 \qquad j = 0, \ldots, \frac{N}{2} \tag{3.11}$$

or

$$P(\nu) = \frac{2}{N_{\mathrm{Ph}}}\left|\sum_{k=1}^{N_0} x_k \mathrm{e}^{-2\pi\nu_j \mathrm{i} t_k}\right|^2 \tag{3.12}$$

$$= \frac{2}{N_{\mathrm{Ph}}}\left[\left(\sum_k x_k \cos(2\pi\nu t_k)\right)^2 + \left(\sum_k x_k \sin(2\pi\nu t_k)\right)^2\right] \tag{3.13}$$

using the normalization after Leahy et al. (1983a). This normalization is usually applied to keep statistics as simple as possible. If the noise in the (equally spaced) time series follows a Poisson distribution (Poisson, 1837), then the distribution of the $P_{j,\mathrm{noise}}$ equals the χ^2 distribution (Helmert, 1876) with 2 degrees of freedom (exponential distribution). The mean power as well as the standard deviation equals 2. In practice we find that this is approximately the case for almost all types of noise. There are also other normalization methods, e.g. by a regularly used one by Miyamoto et al. (1992).

3.4 Problems in Timing Analysis

Now that we have a definition of both the theoretical, continuous Fourier transform and the discrete transform of our observed time series, we also have to consider the caveats of this step in our analysis: when going from the infinite, continuous light curve $x(t)$ emitted by the light source to our finite, in single observations discretely sampled observation of it, we basically have the product of $x(t)$, a "window function"

$$w(t) = \begin{cases} 1, & 0 \leq t < T, \\ 0, & \text{otherwise} \end{cases} \tag{3.14}$$

and a "sampling function"

$$i(t) = \sum_{k=-\infty}^{\infty} \delta\left(t - \frac{kT}{N}\right) \tag{3.15}$$

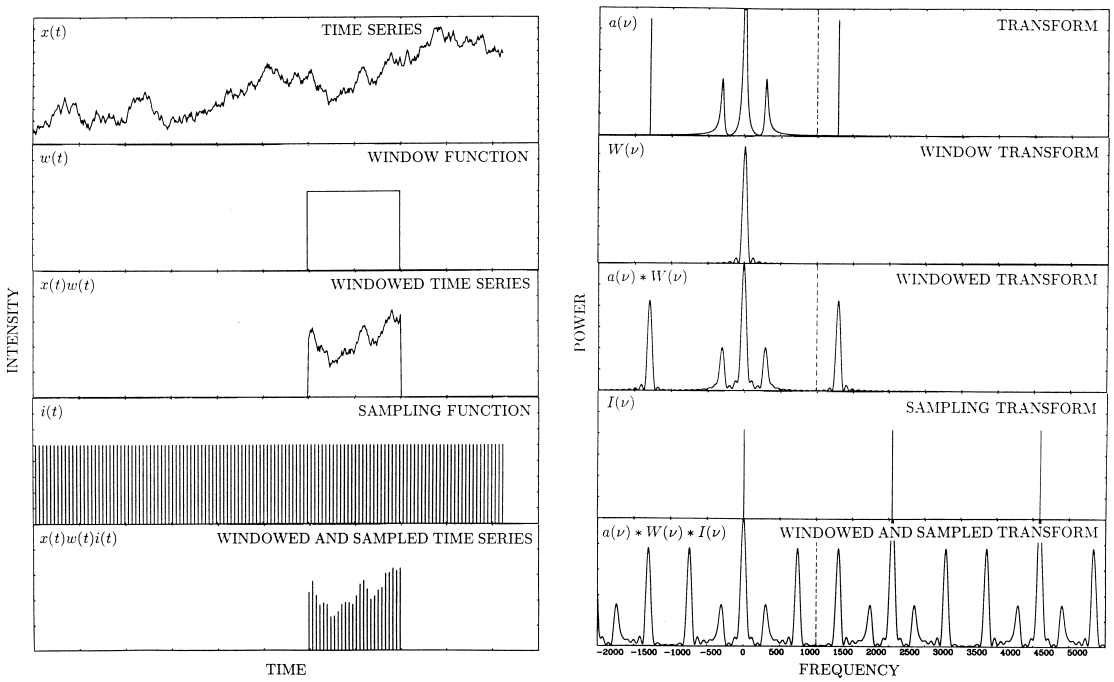

Figure 3.1: Windowing and sampling problems, van der Klis (1989), Fig. 2.2

with the Dirac delta function $\delta(t)$ (Fig. 3.1, left).

Thus, we need the Fourier transform not of a single function $x(t)$ but of the product $x(t)w(t)i(t)$ with its individual Fourier transforms $a(\nu)$, $W(\nu)$, and $I(\nu)$. The convolution theorem states that the Fourier transform of the product of two functions is the convolution of the Fourier transforms of the individual functions. In this case, this means a double convolution of $a(\nu)$ with both

$$W(\nu) = \int_{-infty}^{\infty} w(t) e^{2\pi\nu i t} \mathrm{d}t = \frac{\sin \pi\nu T}{\pi\nu} \tag{3.16}$$

for a symmetric window and

$$I(\nu) = \int_{-\infty}^{\infty} i(t) e^{2\pi\nu i t} \mathrm{d}t = \frac{N}{T} \sum_{l=-\infty}^{\infty} \delta\left(\nu - \frac{lN}{T}\right). \tag{3.17}$$

As a final "windowed and sampled" Fourier transform (Fig. 3.1, right) we get then

$$a_{WI}(\nu) = a(\nu) \otimes W(\nu) \otimes I(\nu) = \int_{-\infty}^{\infty} x(t) w(t) i(t) e^{2\pi i \nu t} \mathrm{d}t \tag{3.18}$$

$$= \int_{-\infty}^{\infty} x(t) \sum_{k=0}^{N-1} \delta\left(t - \frac{kT}{N}\right) e^{2\pi i \nu t} \mathrm{d}t = \sum_{k=0}^{N-1} x\left(\frac{kT}{N}\right) e^{2\pi i \nu \frac{kT}{N}}. \tag{3.19}$$

The effects of these convolutions can be summarized as spectral leakage: The convolution with the window function transform makes all features in $a(\nu)$ become wider, especially

the delta functions that become a wide peak with side lobes (leakage to nearby frequencies). The convolution with the sampling function transform makes all features repeat every N/T frequency units (leakage to distant frequencies). Thus, the simple fact that we are looking at a source only at certain times for a certain length of time makes the periodogram considerably more difficult.

To make things even worse, there is also leakage from high to low frequencies: The power spectrum being symmetric around $\nu = 0$, the power spectrum of the convolution $a(\nu) \otimes I(\nu)$ is reflected at the Nyquist frequency. All features with a frequency higher than $\nu_{N/2}$ are also found in the power spectrum below $\nu_{N/2}$. This effect is called aliasing.

As in practice our sampling of $x(t)$ is not in delta functions but rather in time bins of a finite width δt, and thus the time series is "averaged" over the time bins, high frequency features are damped from the beginning and the aliasing problem is less serious.

In order to keep a power spectrum as simple as possible in the region of interest, there are several methods that can lessen the effects of frequency leakage. The probably most basic method is to apply a low- or high-pass filter to the time series prior to calculating the Fourier transform and thus eliminating influence of unwanted frequencies. This can be achieved using a moving average: Each average value is calculated by subsequent subsets of the time series. Taking the averages is a low-pass filter, subtract the averages from the original values and only taking the high frequency residuals is a high-pass filter. There are simple as well as weighted forms of a moving average.

Another method is called tapering: to lessen the leakage to nearby frequencies caused by the windowing effect, it is possible to use a window function different from the basic rectangular version given in eq. 3.14. Different forms of window functions (e.g., windows that just smooth the corners of a rectangular window, triangular or bell-shaped windows etc.) result in different sidelobe levels and forms in the Fourier transform. However, tapering data also can lead to loss in sensitivity and resolution and should be applied only with special care.

3.5 Lomb-Scargle Method

In astronomy we often have to deal with (more or less) unevenly sampled time series. For such datasets, the simple statistics as in Sec. 3.3 do not hold. Scargle (1982) therefore proposed a modified definition of a periodogram to obtain the same exponential distribution:

$$P(\nu) = \frac{1}{2}\left(\frac{\left[\sum_k x_k \cos(2\pi\nu(t_k - \tau))\right]^2}{\sum_k \cos^2(2\pi\nu(t_k - \tau))} + \frac{\left[\sum_k x_k \sin(2\pi\nu(t_k - \tau))\right]^2}{\sum_k \sin^2(2\pi\nu(t_k - \tau))} \right) \tag{3.20}$$

where

$$\tau = \frac{1}{4\pi\nu} \tan^{-1}\left(\frac{\sum_k \sin(4\pi\nu t_k)}{\sum_k \cos(4\pi\nu t_k)} \right). \tag{3.21}$$

He states that though the outer form of the definition seems to be changed significantly, the actual values of the periodogram are typically not changed much. This modified form of the classical periodogram now is equivalent to the least square fitting of sine waves of the frequencies ν to the data as presented by Lomb (1976). The complicated formula is time translation invariant and can be reduced to the classical periodogram for the case of even sampling. Computing the modified periodogram is not substantially more difficult than is its classical version as there exist similar $\mathcal{O}(N \log N)$ algorithms, e.g. by Press & Rybicki (1989).

This makes the algorithm perfectly suitable to be applied to data from monitoring campaigns where observations are made only on a semi-regular basis. It was implemented to the **I**nteractive **D**ata **L**anguage (IDL) by Jörn Wilms in 2000 and transcribed by myself for use in ISIS in the course of this work. It is publicly available in the isisscripts, a collection of software distributed by the ECAP at www.sternwarte.uni-erlangen.de/isis.

If I can't picture it, I can't understand it.

(Albert Einstein)

4 Probing Periodograms

As the companion star of GRS 1758−258 is not known and the spectral behavior of the compact object is in some points rather peculiar, it seems obvious to use the monitoring data for time series analysis. Information about the binary companion as might be gained of an orbital period might give constraints on the accretion geometry and thus help to find an explanation for the unusual dim soft states the source is showing.

For the time series analysis we used the flux light curve of GRS 1758−258 as shown in Fig. 2.7: as opposed to the count rate, flux values are independent of the respective spectral shape of GRS 1758−258. Due to the many gaps and uneven spacing of the data points, we used the Lomb and Scargle algorithm as described in the previous section.

This analysis was performed before by Smith et al. (2002) on a less extensive dataset. They applied a high-pass filter to the dataset and found a modulation with a period of 18.45 ± 0.10 days. To test the significance of this period, they analyzed 1000 different permutations of their dataset, none of them showing a so high a peak in the power spectrum. They justify the usage of a high-pass filter by analyzing light curves containing artificial signal with the same amplitude as the real ones and finding a peak in the PSD only after filtering.

Smith et al. (2002) find their result compatible with the companion proposed by Marti et al. (1998), a K0 III giant almost exactly filling its Roche lobe (Smith et al., 2000; Rothstein et al., 2002). However, newer astrometric solutions suggest the companion to be an early A-type main sequence star with unusual colors (Muñoz-Arjonilla et al., 2010). As this identification is still ambiguous (Smith, 2010) and, however unlikely, Muñoz-Arjonilla et al. (2010) do not exclude an extra-galactic origin of GRS 1758−258, and as there is a much larger dataset available now as it was for Smith et al. (2002), a new analysis might shed light on this inconsistency.

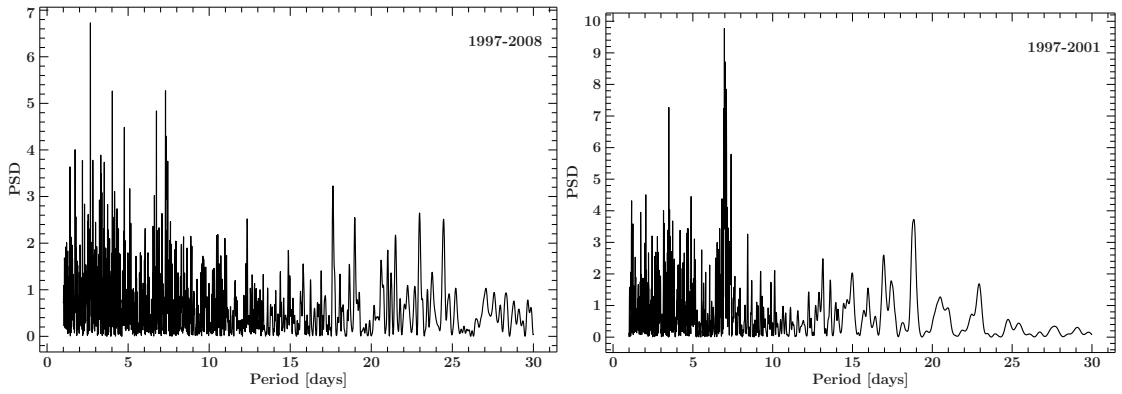

Figure 4.1: *Left:* power spectrum of the complete, unfiltered light curve; *right:* power spectrum of the unfiltered 1997–2001 data already used by Smith et al. (2002).

4.1 The Flux Light Curve and its Periodogram

Applying the Lomb Scargle algorithm to the unfiltered flux light curve, as expected, led to a power spectrum without any prominent peaks. As Smith et al. (2002) reported a 18.45± 0.10 days period for the data between 1997 and 2001, we calculated a periodogram also for this part of the dataset. Again, there are no prominent peaks in the power spectral density (Fig. 4.1). The large luminosity variations between hard and soft spectral states can decrease the significance of period measurements and therefore cause the lack of such peaks (Smith et al., 2002).

4.2 The Detrended Flux Light Curve and its Periodogram

To avoid any influence of the seven dim, almost off soft states on our periodogram, we only used data points where GRS 1758−258 was in the hard state, i.e., with a photon index $\Gamma < 2$ (see Sect. 2.2). However, this step alone is not sufficient to remove long-term

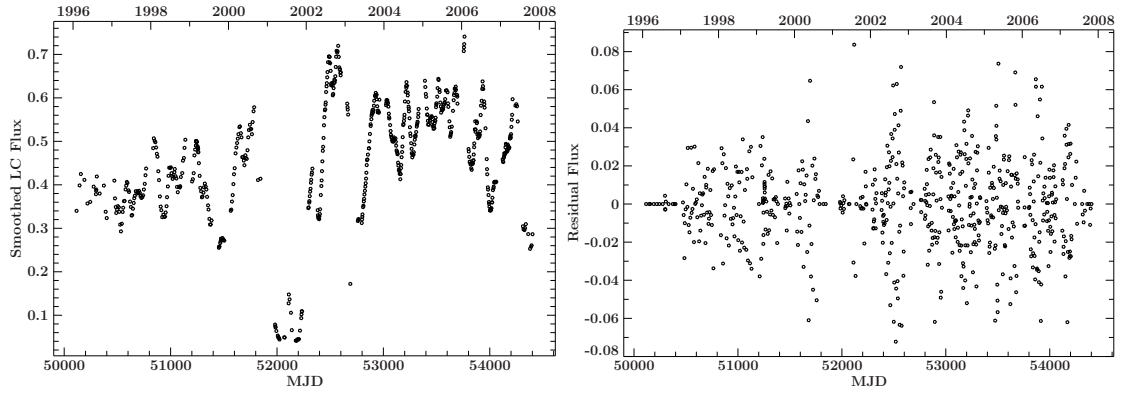

Figure 4.2: *Left:* smoothed light curve and *right:* residual flux in $\mathrm{keV\,s^{-1}\,cm^{-2}}$ of the model flux light curve (see Fig. 2.7) after application of the high-pass filter.

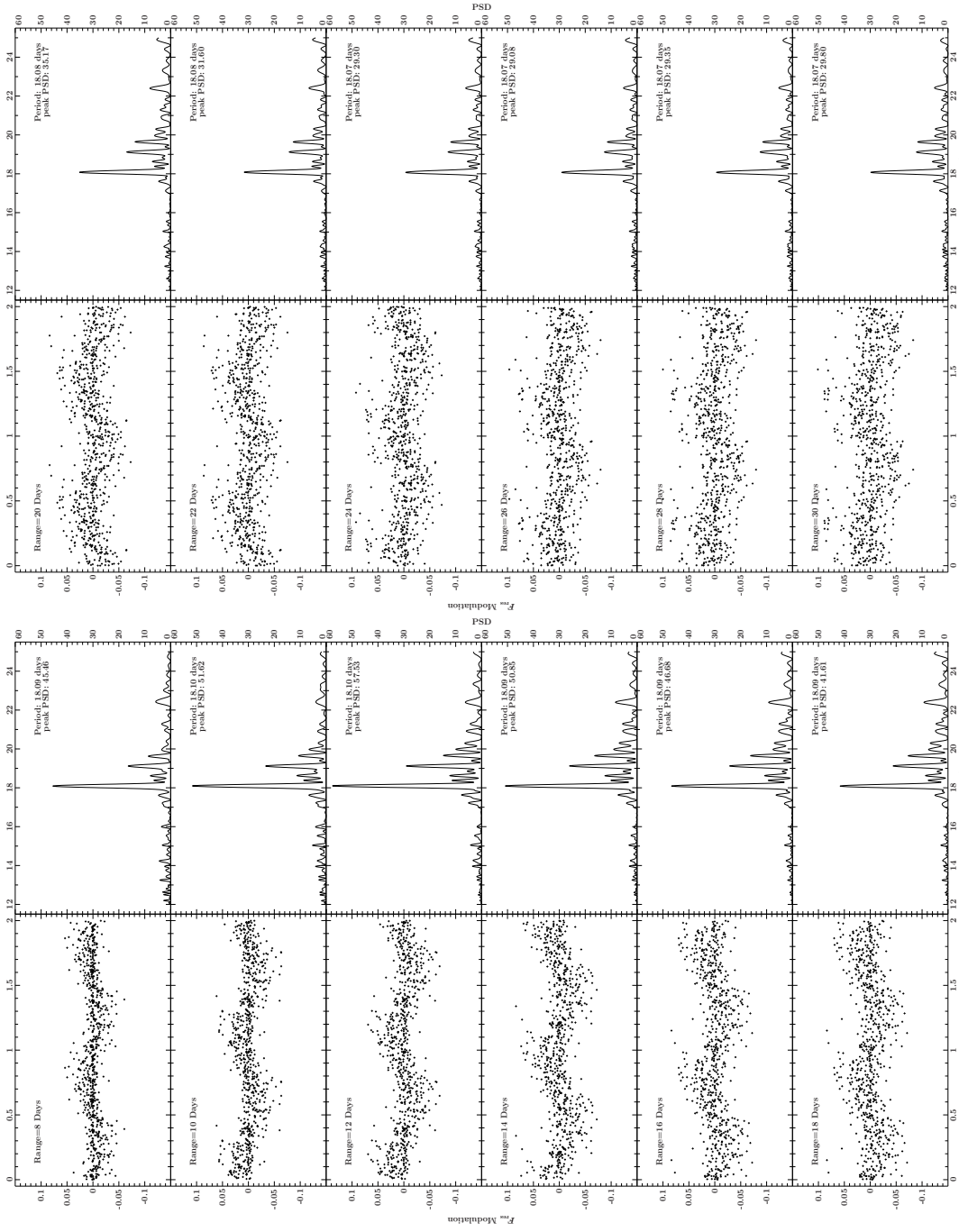

Figure 4.3: Folded light curve (left columns) and power spectrum (right columns) of a central part of the flux light curve for different running average ranges n.

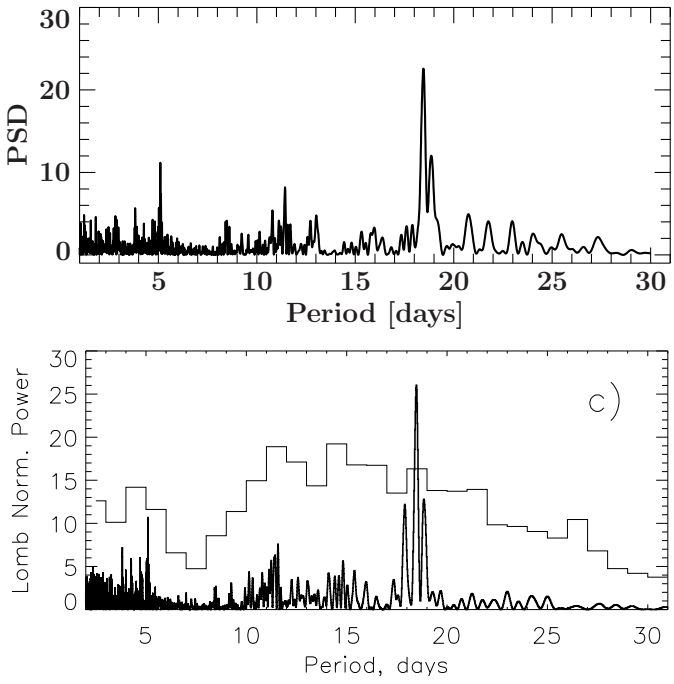

Figure 4.4: *Upper panel:* power spectrum of the 1997–2001 data as used by Smith et al. (2002) as in Fig. 4.5. We are able to reproduce their previous results. *Lower panel:* power spectrum obtained by Smith et al. (2002). The coarse PSD represents the highest values achieved by analyzing scrambled data (Smith et al., 2002, Fig. 2c).

variations. The according PSD still does not show a signal. To avoid lower significances of our measurements caused by large luminosity variations and to be able to compare our results to those of Smith et al. (2002), a high-pass filter was then applied to the data by subtracting a smoothed version of the light curve. The residual flux light curve is shown in Fig. 4.2. All following time series analysis was performed on these high frequency residuals.

To generate the smoothed light curve, for each data point we fitted a straight line to all data within the range of $n = 14$ days before and after. Then we only used the high frequency residual, i.e., the difference between the data point and the value of the straight line to obtain a high-pass-filtered light curve. This method was already applied by Smith et al. (2002) who used a range of $n = 10$ days before and after the data point. We extended this range to reduce the degrees of freedom of the smoothing fit (Fig. 4.3): For too short a range, the many degrees of freedom result in a line at zero. Choosing too large a range reduces the power in the PSD peak, probably due to a beat between period and range. $n = 14$ days appears to be the best compromise in not too many degrees of freedom and large PSD peak height.

Using data from 1997 to 2001, thus, in the same time range as Smith et al. (2002) , we are able to reproduce the peak they found at 18.45 ± 0.10 days within the uncertainties (Fig. 4.4): although we did not exclude the low energy flux where no modulations are expected, we find a peak at 18.475 ± 0.017 days.

However, when using the whole 11 years of data, this peak is shifted in period by 0.32 days (Fig. 4.5, left). Analyzing the data from 2002–2008, i.e. all data after the interval used by Smith et al. (2002) and therefore statistically independent from their sample, the shift increases to 0.33 days. This difference is indicative for a quasi-periodic

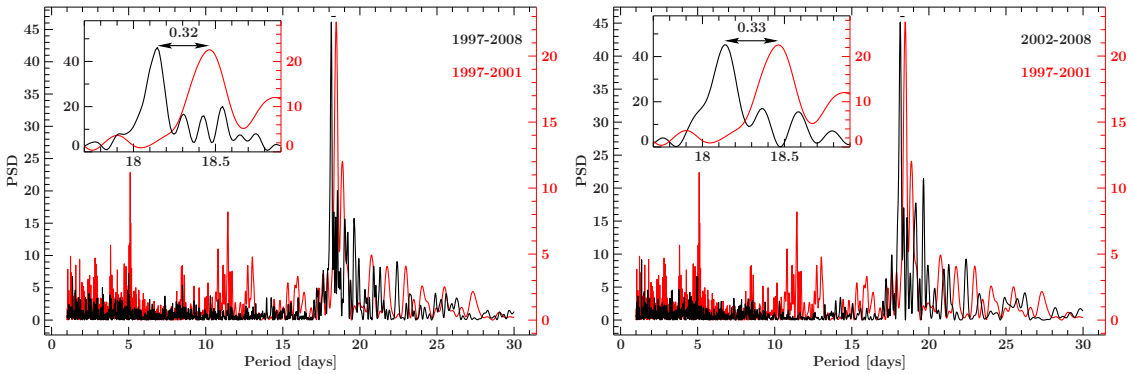

Figure 4.5: Power spectrum of the 1997–2001 data as used by Smith et al. (2002) (red) and power spectrum of the whole light curve (black, left panel) and of the 2002–2008 light curve (black, right panel). The peaks show a difference in period of 0.32 days and 0.33 days, respectively.

oscillation (QPOs, Smith, priv.comm.). To study the evolution of the quasi periodic signal, we calculated a dynamic power spectrum (Fig. 4.6 Benlloch et al., 2001): based on the 5 years interval of data originally used by Smith et al. (2002), slices of the same length of 5 years were cut out of the light curve and analyzed separately. Each time the starting time of the slice was shifted by 30 days, and each resulting power spectrum is shown as a color-coded line in Fig. 4.6. Note that the 83 individual slices are overlapping and thus not statistically independent.

As expected, the first few lines of the dynamic periodogram show a peak at 18.475 ± 0.017 days. The maximum of this peak, however, is drifting with time, first to lower values to a minimum of 18.043 ± 0.005 days in 2003. Towards the end of the light curve, the period of the main peak is rising again. In addition, there seems to be a split in period between 2000 and 2002.

4.2.1 Period Uncertainties

The period uncertainties were calculated by Monte Carlo simulations of light curves containing Poisson noise and an artificial signal close to 18 days to get comparable results but not close enough to interfere with the variability on the original time scale. We chose a sinusoid with a period of 16 days.

First, only this artificial sinusoid was added to the long-term trend of the light curve. The resulting light curve was then filtered and analyzed as above. The amplitude of the 16-day sinusoid was adapted so the resulting peak in the periodogram matches in height the peak of the original data periodogram. The centroid value of the 16-day peak was then determined by fitting a Gaussian to the region immediately around the peak.

Then, for 1000 times an extra set of Poisson fluctuations was added to each data point of the light curve containing the artificial 16-day signal. The light curve was analyzed again and the centroid value of a Gaussian fit to the artificial signal peak was determined. The

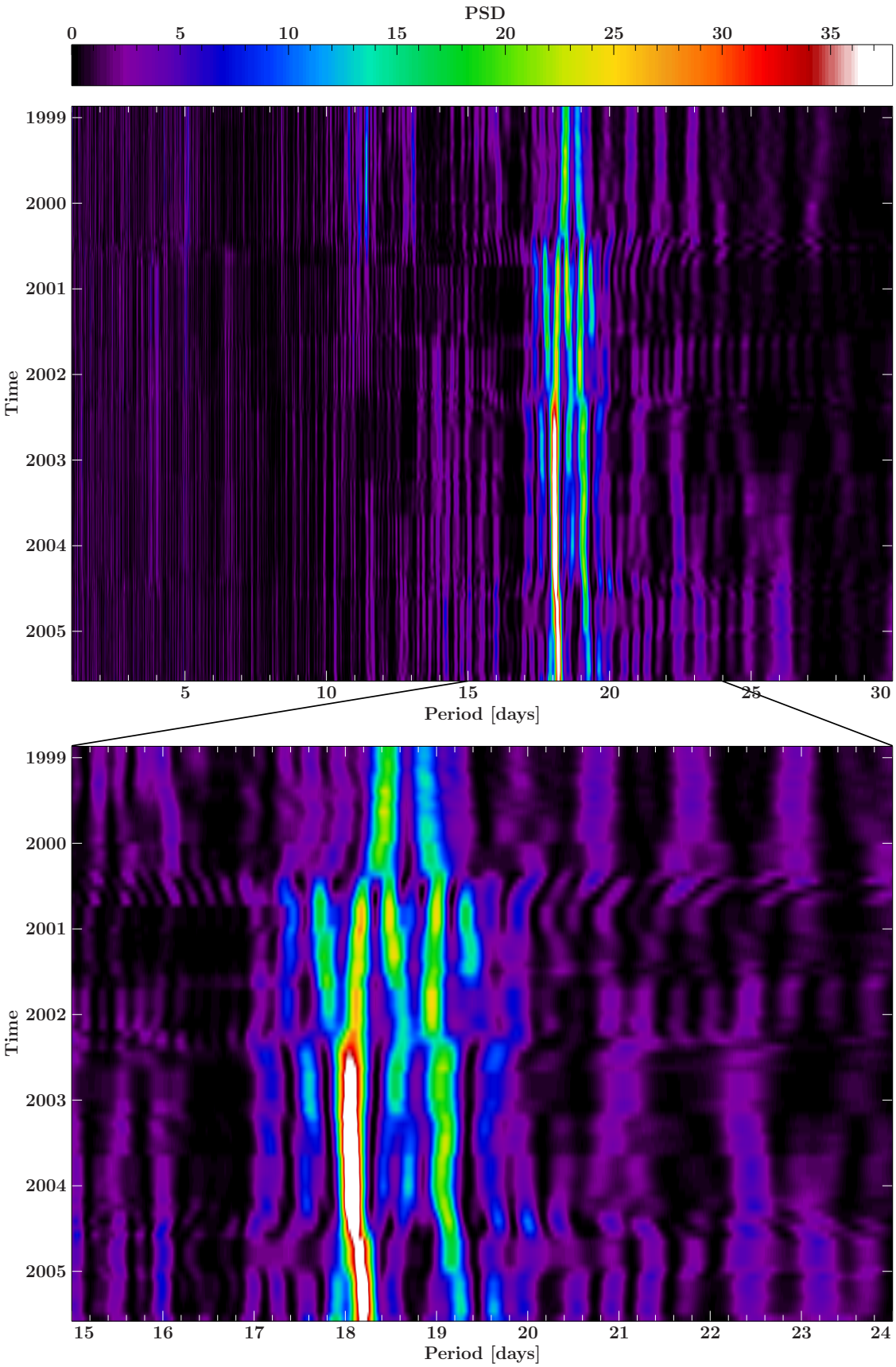

Figure 4.6: Dynamic Lomb-Scargle periodogram for the entire 11 year model flux light curve of GRS 1758−258. The periodogram is calculated in five year intervals (centered on the middle in the time axis), stepped in intervals of 30 days.

Table 4.1: Period, uncertainty and significance for each slice of the dynamic power spectrum.

Date [MJD]	Period [days]	Significance [%]	Date [MJD]	Period [days]	Significance [%]
50470.955–51844.411	18.475 ± 0.017	99.18	51715.808–53167.240	18.077 ± 0.028	99.36
50484.694–51844.411	18.464 ± 0.017	99.17	51744.599–53198.498	18.066 ± 0.004	99.94
50513.179–51844.411	18.464 ± 0.014	99.27	51771.223–53229.454	18.043 ± 0.007	99.82
50541.524–51996.672	18.464 ± 0.014	99.30	51821.229–53255.388	18.054 ± 0.010	99.75
50576.740–52027.629	18.452 ± 0.007	99.54	51844.411–53286.016	18.054 ± 0.006	99.84
50604.228–52058.720	18.4523 ± 0.0023	99.74	51970.948–53319.473	18.0541 ± 0.0014	99.95
50633.364–52089.014	18.441 ± 0.010	99.48	51970.948–53331.016	18.0541 ± 0.0012	99.93
50663.646–52118.414	18.452 ± 0.014	99.35	51970.948–53331.016	18.0541 ± 0.0012	99.93
50694.256–52145.356	18.43 ± 0.04	98.68	51970.948–53407.897	18.0541 ± 0.0013	99.96
50721.674–52176.558	18.42 ± 0.04	98.66	51981.879–53439.175	18.0541 ± 0.0015	99.94
50756.891–52209.272	18.43 ± 0.05	98.15	52011.059–53462.430	18.0428 ± 0.0016	99.92
50835.984–52235.396	18.43 ± 0.05	98.18	52041.685–53498.683	18.043 ± 0.005	99.82
50835.984–52235.396	18.43 ± 0.05	98.18	52072.432–53528.510	18.054 ± 0.011	99.59
50842.118–52297.686	18.42 ± 0.05	98.23	52099.602–53558.618	18.054 ± 0.012	99.66
50870.524–52328.292	18.384 ± 0.029	98.91	52129.340–53587.852	18.054 ± 0.004	99.76
50899.210–52359.585	18.373 ± 0.029	99.18	52161.599–53610.388	18.0541 ± 0.0010	99.96
50931.885–52387.517	18.37 ± 0.04	98.64	52189.215–53642.772	18.0541 ± 0.0009	99.97
50961.824–52419.303	18.361 ± 0.028	99.21	52219.799–53679.901	18.0655 ± 0.0018	99.97
50994.697–52445.507	19.021 ± 0.022	99.42	52294.647–53696.213	18.0769 ± 0.0020	99.87
51019.156–52479.391	19.033 ± 0.029	99.24	52294.647–53696.213	18.0769 ± 0.0020	99.87
51054.369–52509.206	19.021 ± 0.028	99.27	52311.322–53762.474	18.0769 ± 0.0014	99.98
51080.027–52538.557	19.0098 ± 0.0026	99.82	52339.266–53762.474	18.0769 ± 0.0021	99.83
51109.297–52568.911	18.475 ± 0.016	99.57	52382.170–53825.821	18.0769 ± 0.0013	99.98
51201.727–52598.253	18.179 ± 0.004	99.86	52402.699–53859.867	18.0769 ± 0.0021	99.88
51201.727–52600.015	18.179 ± 0.006	99.74	52430.605–53888.966	18.077 ± 0.007	99.78
51201.727–52659.850	18.179 ± 0.007	99.73	52461.479–53917.705	18.0883 ± 0.0012	99.96
51230.637–52689.211	18.1679 ± 0.0022	99.86	52493.256–53948.756	18.088 ± 0.008	99.77
51260.025–52694.875	18.1452 ± 0.0013	99.93	52521.987–53975.985	18.0883 ± 0.0009	99.96
51294.071–52694.875	18.1452 ± 0.0023	99.84	52552.189–54007.040	18.010 ± 0.006	99.82
51321.668–52779.859	18.532 ± 0.005	99.83	52580.727–54036.954	18.1452 ± 0.0017	99.94
51351.912–52809.238	18.532 ± 0.006	99.81	52659.850–54061.384	18.157 ± 0.004	99.80
51385.011–52839.961	18.145 ± 0.013	99.64	52659.850–54061.384	18.157 ± 0.004	99.80
51410.783–52868.359	18.134 ± 0.014	99.59	52676.054–54126.934	18.1565 ± 0.0027	99.76
51441.015–52898.732	18.111 ± 0.008	99.74	52755.521–54154.236	18.1679 ± 0.0030	99.78
51469.445–52928.019	18.1110 ± 0.0012	99.92	52755.521–54188.916	18.179 ± 0.010	99.60
51504.242–52958.200	18.122 ± 0.016	99.57	52759.745–54214.726	18.191 ± 0.004	99.83
51564.807–52962.648	18.122 ± 0.020	99.44	52791.302–54249.485	18.1907 ± 0.0027	99.85
51564.807–52962.648	18.122 ± 0.020	99.44	52821.886–54269.190	18.191 ± 0.004	99.83
51589.966–53047.182	18.111 ± 0.021	99.56	52849.827–54304.276	18.202 ± 0.008	99.76
51624.536–53078.187	18.122 ± 0.026	99.15	52879.804–54339.078	18.202 ± 0.010	99.54
51651.751–53107.394	18.111 ± 0.029	99.18	52911.282–54367.423	18.191 ± 0.004	99.73
51680.666–53138.053	18.088 ± 0.030	99.24			

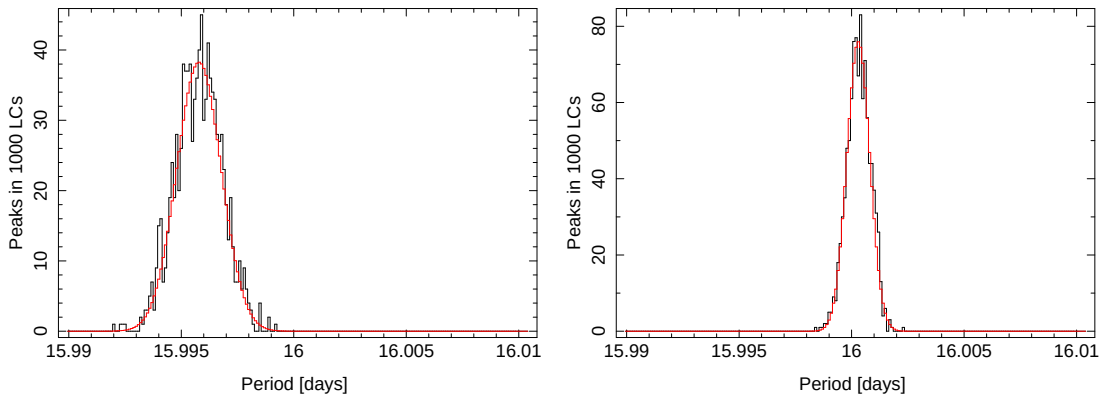

Figure 4.7: Two examples for the distribution of peaks of the 1000 fake signal light curves (black histogram). In both cases, the distribution has a Gaussian shape (red histogram).

standard deviation of the distribution of the 1000 simulated peaks around the center of the peak calculated before adding noise is a measure for the uncertainty in the period. Fig. 4.7 shows two examples of the distribution of these peak values. The filtering process seems to slightly shift the peak period values with respect to the original fake signal, depending on the light curve slice. However, this shift is by definition within the calculated uncertainty. The process leads to conservative uncertainties that are slightly overestimated, as it adds Poisson fluctuations to a light curve that already contains Poisson noise. The significance level of these uncertainties is calculated next.

4.2.2 Period Significances

To estimate the significance of the period, we simulated 10000 light curves consisting of a white noise component with the same standard deviation as the original short-term residuals. For each light curve, a dynamic power spectrum with 83 overlapping light curve slices was calculated in the same way as in Sect. 4.2. We find the period of the highest peak for each light curve slice of the dynamic power spectrum for all of the 10000 simulated light curves. For each slice, we then use the percentage of the simulated light curves that show no peak in the range of the previously found period and its uncertainty in the respective slice as a measure for the significance of said period. We find significances for the drifting peak varying between 98.15% and 99.98% (see Table 4.1).

4.2.3 Systematic Effects

Although our high-pass filter works well for detecting periodic signals in the data, it is not ideal: when calculating uncertainties for the period (see Sect.4.2), we found that the long-term trend the filter is supposed to remove still contains part of periodic signals in the range of 14 to 25 days. As the period found by Smith et al. (2002) falls in this range, we took a closer look into the origin of this effect.

The light curve in which the residual signal appears was produced in the following way:

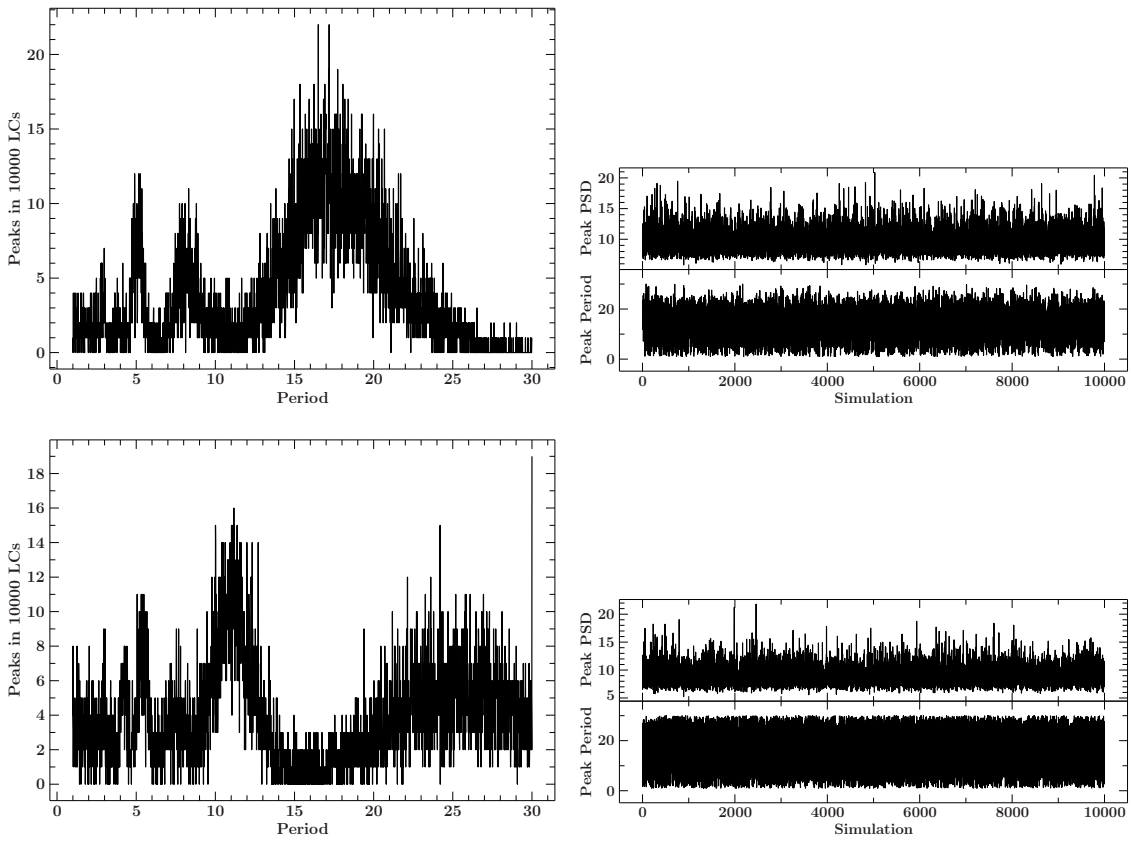

Figure 4.8: Distribution of highest peak periods for the power spectra of 10000 simulated pure white noise light curves for a filter $n = 14$ (top) and $n = 20$ (bottom).

we took a Gaussian noise light curve using the same dates as in the original light curve. We added a primary sinusoidal signal with a period in the range of 14 to 25 days and filtered the light curve to determine the long-term trend. To this trend, we added an additional test signal of a different period, e.g. 12 days, filtered again and applied the Lomb-Scargle technique as in Sect. 4.2. The resulting periodogram shows a main peak at the period of the test signal and a second peak at the period of the primary sinusoidal period.

As in this analysis we initially used a pure noise light curve and not the long-term trend of the data, the residual signal is not connected to the flux values in our light curve. Neither changing the period of the test signal nor changing the length of the light curve section we use has any influence on this effect. Using only randomly selected two thirds of the data points in the light curve lessens the effect but also reduces the height of the test signal peak in the periodogram. The distribution of time intervals between individual observations does not show an excess for intervals between 14 and 25 days. We therefore exclude that the periodicity found in the data is the result of the sampling of our light curve.

However, the range in which the residual signal appears shifts according to the filter range n, and is always located between n and $2n$ (Fig. 4.9). Thus, we conclude that this

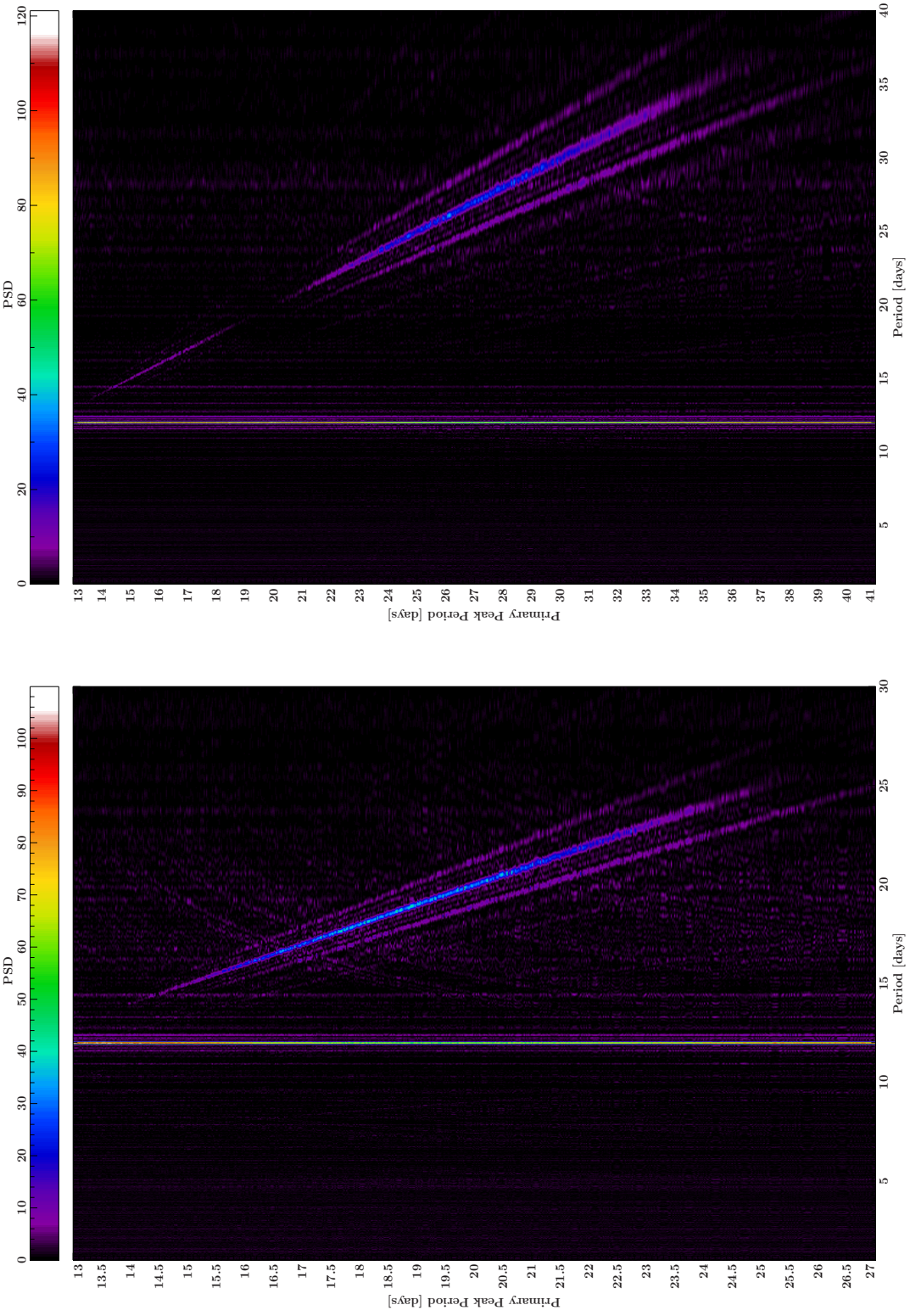

Figure 4.9: Residual signal after high-pass filter for a filter length of $n = 14$ (left) and $n = 20$ (right). For a slice of the light curve, a primary signal was added at different periods, the secondary signal always located at $p = 12$ days. Sidelobes are clearly visible.

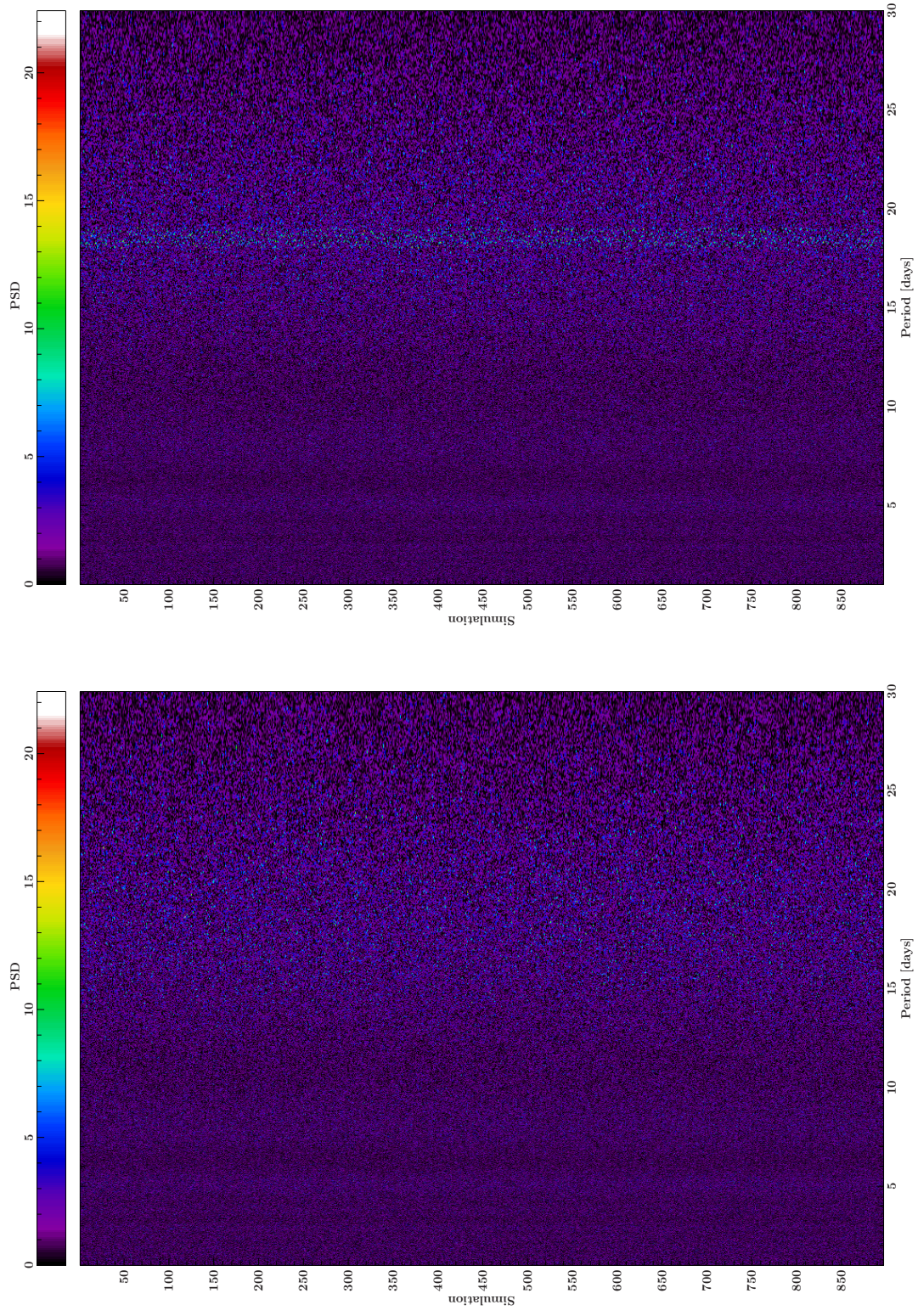

Figure 4.10: Dynamic power spectra of the first 897 of 10000 simulated pure white noise light curves (left) and of the 897 light curves out of the 10000 sample that show their highest peak between 18 and 19 days (right). Peaks are not prominent.

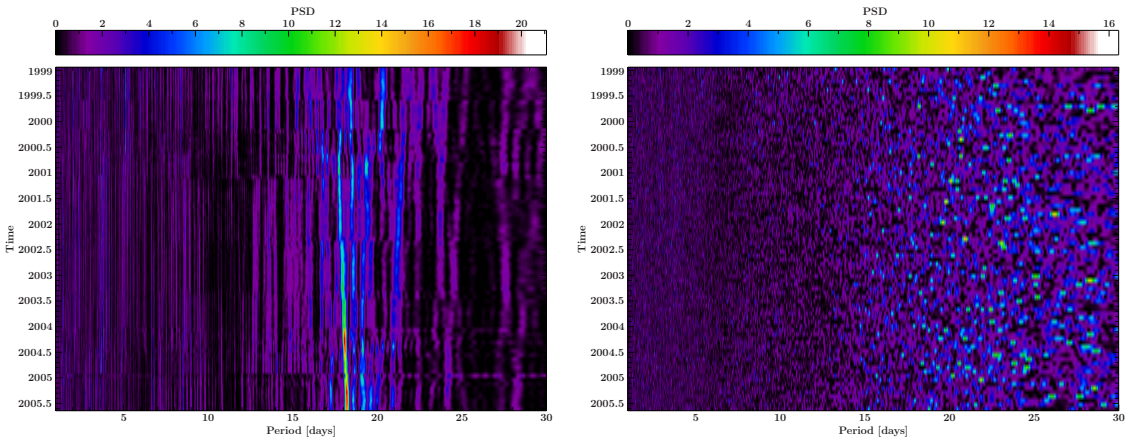

Figure 4.11: Dynamical power spectrum of a simulated red noise light curve with (left) and without (right) the original long-term trend.

residual signal is left because the filter is not an ideal high pass. But as we find a significant peak in the periodogram although the filter removes part of the signal together with the long-term trend, this filter effect does not impair the main results of our analysis.

In addition, we tested if the drifting peak in the periodogram could be caused by the filtering process: we took a pure white noise light curve with the original sampling. The standard deviation of the white noise random numbers equals the standard deviation in the original residual light curve. We filtered out the "long-term trend" and calculated a dynamic power spectrum of the short term residuals. Fig. 4.8 shows the distribution of the highest peaks in the simulated power spectra. For a filter with $n = 14$ days, 8.97% of the simulated white noise light curves show their largest peak in the power spectrum between 18 and 19 days. This is expected as the filter is supposed to be sensitive to exactly these periods: taking a closer look at these power spectra (Fig. 4.10) we see that these peaks are not nearly as prominent as the one we found in the original data. However, when using a filter with $n = 20$ days for comparison, the accumulation moves from between 15 and 20 days to above 20 days (Fig. 4.8). Thus, what we see here is the approximate filter response.

To determine whether the shifting peak is real, we also tested for red noise effects: red noise values were taken out of the middle of a simulated red noise light curve (Timmer & Koenig, 1995) with 100000 data points to avoid windowing effects of the simulation routine. These values were then added as a red noise component to the smoothed GRS 1758−258 light curve. This final simulated red noise light curve was then analyzed in the same way as the real data, again using a high-pass filter before applying the Lomb Scargle algorithm. The dynamical power spectrum of the light curve containing the long-term trend and additional red noise (Fig. 4.11, left) shows the period residuals as explained above. Simulating just the red noise without the original long-term trend, the resulting dynamic power spectrum (Fig. 4.11, right) does not show any peak at all in the period range we are interested in. We therefore can exclude a red noise origin for the drifting peak.

An expert is a person who has made all the mistakes that can be made in a very narrow field.

(Niels Bohr)

5 Concerning Conclusions

Using the model flux light curve for timing analysis, we are not able to detect any orbital modulation in the dataset. However, calculating a dynamic power spectrum based on the modulation found by Smith et al. (2002) reveals a peak drifting between 18.47 ± 0.11 and 18.04 ± 0.50 days with a significance between 96.2 and 99.95%. Even though we did not find a constant orbital period, a time-varying peak in the dynamical PSD could still be close to the orbit if it is caused by superhump behavior of the accretion disk. An introduction to the formation of superhumps can be found, e.g., in Frank et al. (2002, but see also Pringle; Maloney & Begelman; Ogilvie & Dubus; Haswell et al.):

In X-ray binaries, the accretion disk will be heated by irradiation by the central object. Assuming that central object to be a point source radiating with luminosity L in a spherically symmetric way, the effective temperature T_{Pt} of the disk due to heating at a radius R can be calculated to (Frank et al., 2002)

$$T_{\mathrm{Pt}}^4 = \frac{L}{4\pi R^2 \sigma_{\mathrm{SB}}} \left(\frac{H}{R}\right) \left[\frac{\mathrm{d}\ln H}{\mathrm{d}\ln R} - 1\right] (1-\beta), \tag{5.1}$$

with the Stefan-Boltzmann constant σ_{SB}, the local scale height $H = R\tan\Phi$ (see Fig. 5.1) and an albedo β of the disk. For the special case of a black hole binary, this temperature looks slightly different as the source of radiation is not a point source in the center of the disk but rather the inner disk itself, leading to a smaller solid angle and thus an extra factor $\sim H/R$ (Frank et al., 2002): in such systems, the irradiation effect is weaker.

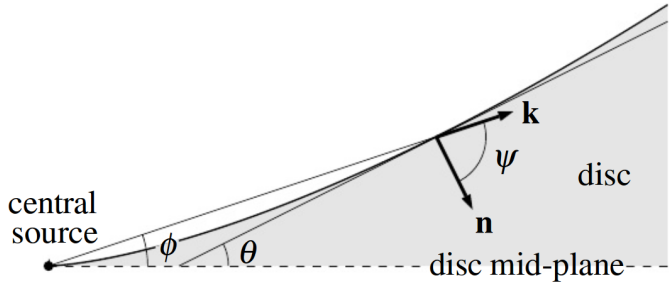

Figure 5.1: Irradiated disk geometry (Frank et al., 2002, Fig. 5.16)

The strong dependence of the temperature on the radius leads to a large range of temperatures in the disk. Thus, in some regions of the disk the temperature can rise above the local hydrogen ionization temperature T_{H}, removing the thermal-viscous instability (see Frank et al., 2002, Section 5.8 for more details): for temperatures below T_{H} hydrogen is only partly ionized and the material tends to clump into rings, leading to variations in the accretion flow and thus in luminosity, as seen, e.g., in dwarf novae (Smak, 1982). If the whole disk is heated above T_{H}, the instability is totally suppressed and we expect a persistent source. If at outer radii the disk temperature stays below this threshold, the source shows outbursts and is classified as a soft X-ray transient (Frank et al., 2002).

However, the heating is not the only effect to consider: as accretion disks are supposed to have an optically thick surface, the irradiated luminosity will be re-emitted or scattered from the disk, resulting in radiation pressure exerting a force

$$\mathrm{d}F = \frac{2}{3}\frac{L}{4\pi R^2 c}\mathrm{d}A \tag{5.2}$$

on an element of area dA, directed along the disk normal n (Fig. 5.1). As long as the disk is ideally symmetric respective to the orbital plane, the forces on both its surfaces equal each other, but as soon as the symmetry is even a little disrupted, a torque is applied on disk material, allowing a net torque leading to precession (Frank et al., 2002, as well as Petterson, 1977, and Iping & Petterson, 1990). If the radiation induced torque outbalances the viscous torque resisting it, this precession then increases the asymmetry and thus the net torque: a warp is formed.

Applying a perturbation analysis as done, e.g., by Pringle (1996) (but see also Maloney et al., 1996; Maloney & Begelman, 1997; Maloney et al., 1998; Wijers & Pringle, 1999; Ogilvie & Dubus, 2001) shows that warping will occur if

$$L \gtrsim 12\pi^2 \nu_2 \Sigma v_\Phi c \tag{5.3}$$

with the vertical viscosity ν_2, the surface density Σ and the azimuthal disk velocity v_Φ (Pringle, 1996, ep. 4.1). Defining the ratio of the vertical viscosity to the radial viscosity ν as

$$\eta = \nu_2/\nu \tag{5.4}$$

and introducing the mass accretion rate for a steady disk

$$\dot{M} = 3\pi\nu\Sigma \tag{5.5}$$

as well as the accretion efficiency

$$\epsilon = \frac{L}{\dot{M}c^2}\left(\simeq \frac{R_*}{R_{\mathrm{S}}}\right) \tag{5.6}$$

we can simplify 5.3 to

$$\frac{v_\Phi}{c} \lesssim \frac{\epsilon}{4\pi\eta} \tag{5.7}$$

(Pringle, 1996). To see the radial dependence of the instability, we can approximate

$$\frac{v_\Phi}{c} = \frac{1}{\sqrt{2}}\left(\frac{R}{R_{\mathrm{S}}}\right)^{-1/2} \tag{5.8}$$

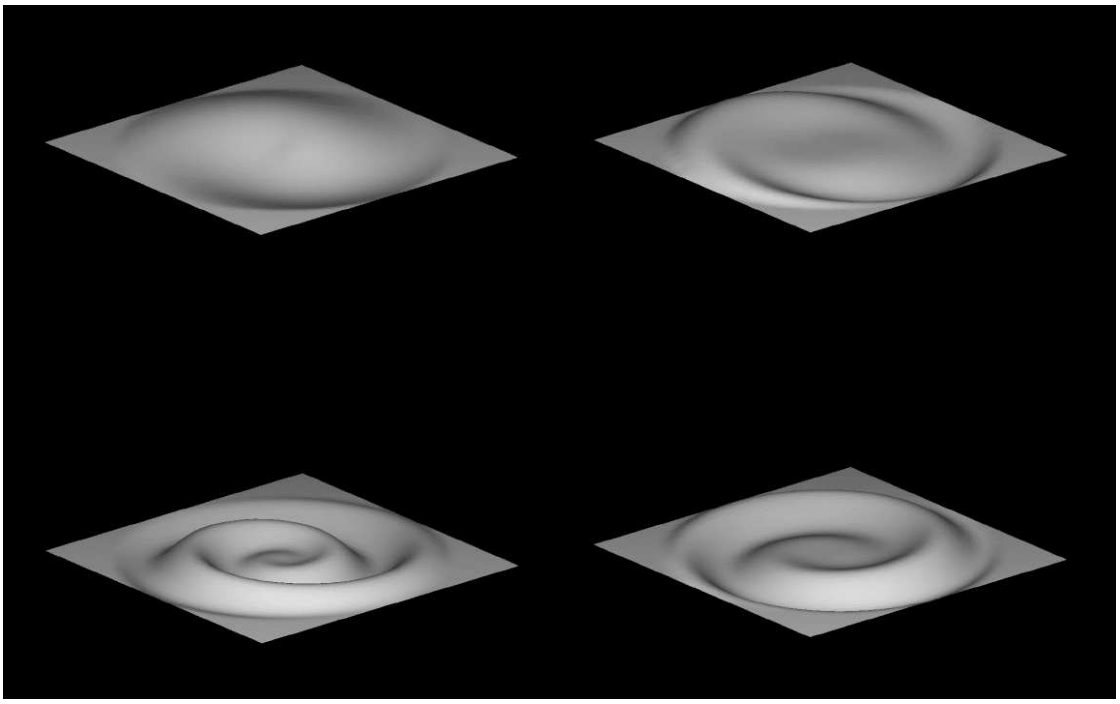

Figure 5.2: Surface plots of different warp modes obtained from numerical calculations (Maloney & Begelman, 1997, Fig. 3).

with the Schwarzschild radius R_S, and see that (Pringle, 1996, eq. 4.3)

$$\frac{R}{R_S} \gtrsim \left(\frac{2\sqrt{2}\pi\eta}{\epsilon} \right)^2 \tag{5.9}$$

or, using equation 5.7

$$\frac{R}{R_*} \gtrsim 8\pi^2\eta^2 \frac{R_*}{R_S} \tag{5.10}$$

We can see that the instability to warping depends on several factors, some of which we can only make assumptions for, e.g., the viscosity (which is however an important quantity as it makes all orbits slightly aperiodic (Frank et al., 2002). Putting in typical numbers for a black hole ($R_* = R_S$, $\eta \sim 1$), we find warping possible at

$$R \gtrsim 8\pi R_S \sim 2.34 \cdot 10^5 \mathrm{m} \cdot \frac{M}{M_\odot} \tag{5.11}$$

In addition, the above calculations can only tell about the initiating of a warp. Its evolution has to be calculated numerically. Figure 5.2 shows an example by Maloney & Begelman (1997) whose calculations also include the influence of an external torque, e.g., by the companion star, but see also Maloney et al. (1998) for nonisothermal disks.

The first observational evidence for such warps are so-called superhumps occuring in SU UMa systems, a class of dwarf novae. These systems from time to time undergo

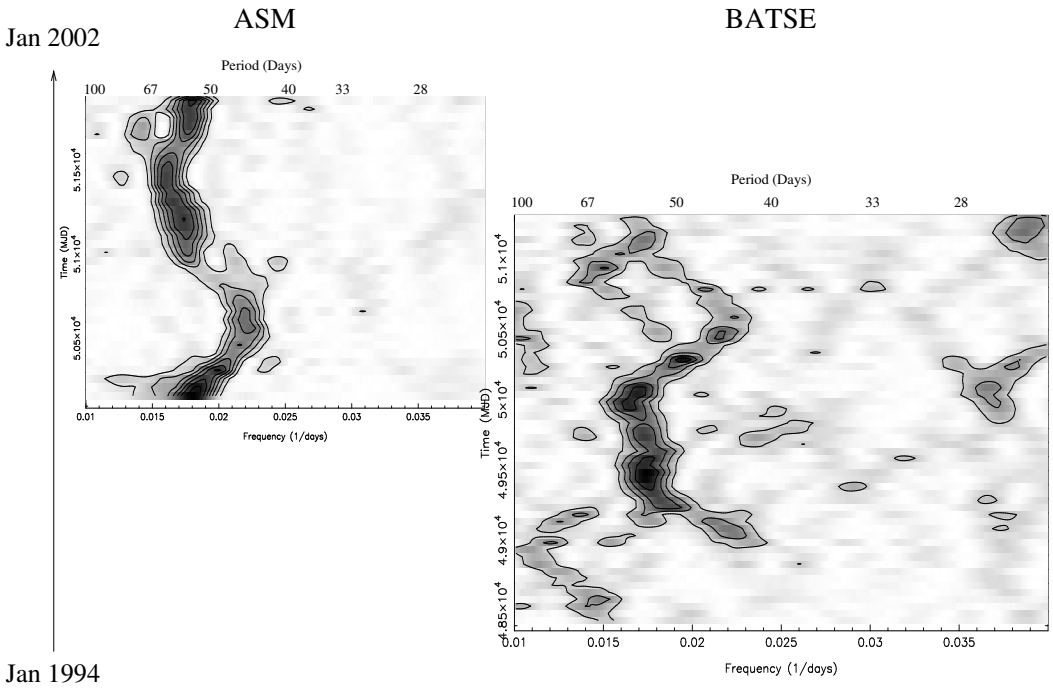

Figure 5.3: Dynamic power spectrum of SMC X-1 observed by the *RXTE* ASM (soft X-rays) and the *CGRO* BATSE (hard X-rays) (Clarkson et al., 2003b)

superoutbursts of a rather long time span (see Warner, 2003, for a review of SU UMa systems and other cataclysmic variables). During such superoutbursts, many sources were observed to show periodic optical oscillations, called superhumps, with a period slightly longer than the systems' orbital periods. These superhumps are due to a 3:1 orbital resonance within the accretion disk, causing the disk to be eccentric and to slowly precess. The luminosity modulation is then caused by periodic variations of the efficiency of dissipative processes in the accretion disk (Whitehurst, 1988; Whitehurst & King, 1991; Lubow, 1991a,b).

Masetti et al. (1996), Haswell et al. (2001) and Charles (2002) review observations of superhumps also in soft X-ray transients and LMXBs. Masetti et al. (1996) suggest another origin for the modulations: with an elliptical disk shape, the accretion flow impacts the outer disk at varying distances from the central object and thus at different gravitational potentials, leading to modulations in the released energy. Other possible mechanisms include a variation in the uncovered area in the direction of the observer or varying absorption by a disk warp.

Based on this, Clarkson et al. (2003b) suggest a similar mechanism to explain the third period of the HMXB SMC X-1, consisting of a neutron star and the B0 I optical companion Sk 160 (Reynolds et al., 1993). Wojdowski et al. (1998) detected a superorbital period in this persistent source. When analyzing a more extensive dataset, Clarkson et al. (2003b)

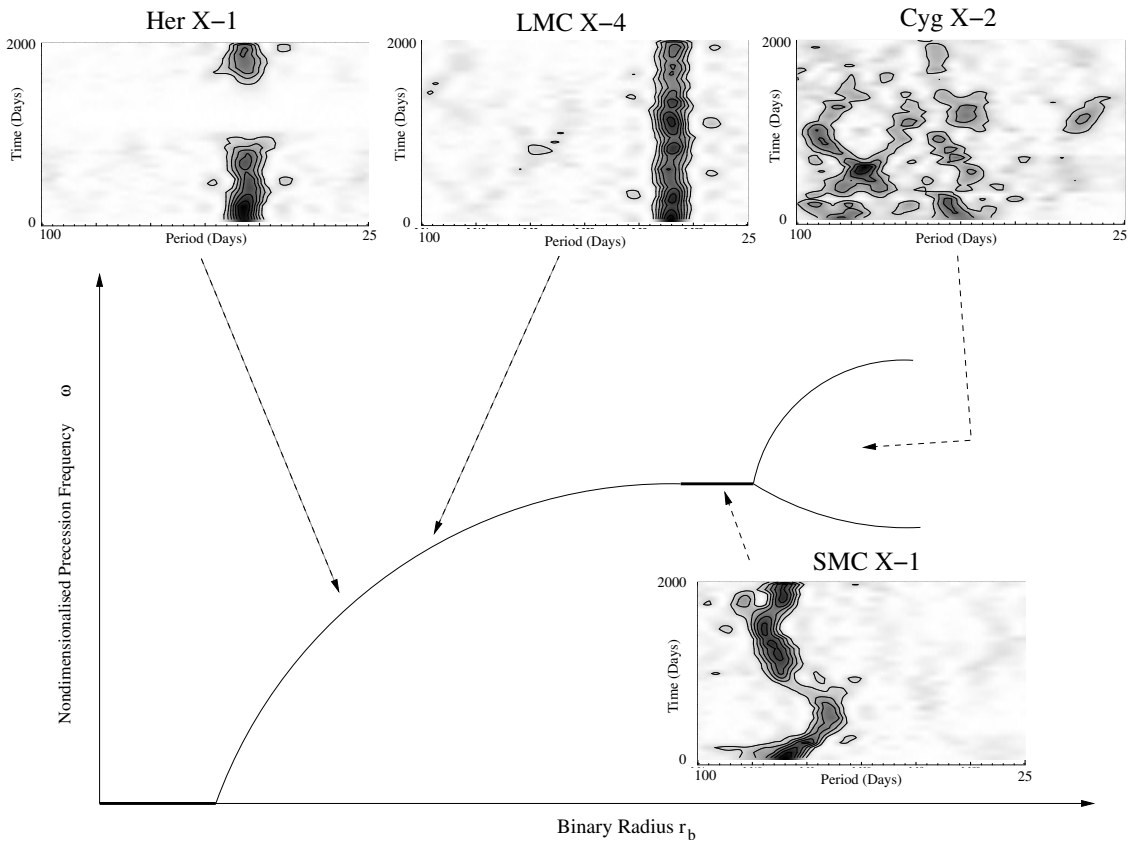

Figure 5.4: (Clarkson et al., 2003a, Fig. 14)

found this period to be varying between 40 and 60 days. They performed an analysis similar to ours, and also their dynamic power spectrum looks quite similar (Fig. 5.3). They suggest the modulation being due to a bright spot at the intersection of accretion flow and accretion disk. This mechanism can support variations in the superorbital period (Clarkson et al., 2003b).

In the subsequent paper, Clarkson et al. (2003a) present the analysis of a sample of other sources showing superorbital periods and put up a scheme, showing the evolution of disk warping with respect to the binary radius (Fig. 5.4). With regard to the predictions of Ogilvie & Dubus (2001) they propose that for very close binaries, warping due to irradiation of the disk is not possible, whereas with increasing separation of the binary components there is one stable warp mode as seen, e.g., in Her X-1 or LMC X-4. Near the boundary to the region with two stable modes, two modes start to compete, resulting in an unstable superorbital period as observed in SMC X-1. Once that boundary is crossed, several strong periodicities interact, e.g., in Cyg X-2.

The result of Clarkson et al. (2003b,a) raises the question whether a similar mechanism is applicable to GRS 1758−258. Both Her X-1 and LMC X-4 accrete via Roche lobe overflow, whereas SMC X-1 is a wind accretor. If the companion of GRS 1758−258 is indeed the A-type star proposed by Muñoz-Arjonilla et al. (2010), the system would probably

be somewhere in between. Thus, we would expect the range of the varying period of GRS 1758−258 accordingly much smaller.

As warping is driven by radiation, we can also compare the luminosities of GRS 1758−258 and SMC X-1. Here, we come to a different result: For SMC X-1 we find an X-ray flux[1] of $F_1 = 4.15 \cdot 10^{-10}\,\mathrm{erg\,s^{-2}\,cm^{-2}}$ (Baumgartner et al., 2013) and a distance d_1 of 60 kpc to 65 kpc (Naik & Paul, 2004; Neilsen et al., 2004, respectively). For GRS 1758−258, the flux is given as $F_2 = 13.63 \cdot 10^{-10}\,\mathrm{erg\,s^{-2}\,cm^{-2}}$ (Baumgartner et al., 2013).

If both sources have the same intrinsic luminosity, from the flux ratio we find that GRS 1758−258 would be located at $d_2 = 33.1 \ldots 35.9$ kpc. This would mean that GRS 1758−258 is situated far behind the Galactic Center and we would expect a very high hydrogen column density in our line of sight. Soria et al. (2011) observe a total column density $N_\mathrm{H} = 1.66 \cdot 10^{22}\,\mathrm{cm^{-2}}$ toward GRS 1758−258, whereas the LAB survey (Kalberla et al., 2005) finds only $N_\mathrm{H} = 7.51 \cdot 10^{21}\,\mathrm{cm^{-2}}$ in this direction. Thus, due to its higher absorption column, GRS 1758−258 could indeed be located at such a distance, or else, could have a companion emitting stellar wind.

However, as we have seen above, there are many factors that influence the formation of warps in an accretion disk, and many mechanisms that lead to an observable variability in the light curve, so that we cannot finally conclude this special mechanism of a warped disk to be the origin of the variable periodicity in GRS 1758−258. Further observations of such systems are needed to have a statistical relevant sample of different superorbital periods and to be able to fit in the scheme sources as GRS 1758−258 where we do not know much about the distance, the companion or the binary separation and orbit.

But for all that, we can at least draw one concrete conclusion from our analysis: The variability on timescales of days as we see it rules out an extra-galactic origin of GRS 1758−258, which was not possible before (Muñoz-Arjonilla et al., 2010).

[1] http://swift.gsfc.nasa.gov/results/bs70mon/

References

Balbus S.A., Hawley J.F., 1991, ApJ 376, 214

Baumgartner W.H., Tueller J., Markwardt C.B., et al., 2013, ApJS 207, 19

Belloni T., (ed.) 2010, The Jet Paradigm: From Microquasars to Quasars, Springer Verlag, Berlin

Benlloch S., Wilms J., Staubert R., Nowak M., 2001, In: Gimenez A., Reglero V., Winkler C. (eds.) Exploring the Gamma-Ray Universe. ESA SP 459, ESA Publications Division, Noordwijk, p.263

Bondi H., Hoyle F., 1944, MNRAS 104, 273

Bradt H.V., Rothschild R.E., Swank J.H., 1993, A&AS 97, 355

Cadolle Bel M., Goldwurm A., Sizun P., 2006, In: Meurs E.J.A., Fabbiano G. (eds.) Populations of High Energy Sources in Galaxies. IAU Symposium 230, Cambridge University Press, p.93

Carroll B.W., Ostlie D.A., 2007, An Introduction to Modern Astrophysics and Cosmology, Second Edition, Pearson Education, Addison Weasley, San Francisco

Casares J., Negueruela I., Ribo M., et al., 2014, ArXiv e-prints

Charles P.A., 2002, In: Gänsicke B.T., Beuermann K., Reinsch K. (eds.) The Physics of Cataclysmic Variables and Related Objects. ASP Conf. Ser. 261, Astron. Soc. Pacific, San Francisco, p. 223

Clarkson W.I., Charles P.A., Coe M.J., Laycock S., 2003a, MNRAS 343, 1213

Clarkson W.I., Charles P.A., Coe M.J., et al., 2003b, MNRAS 339, 447

Coe M.J., 2000, In: Smith M.A., Henrichs H.F., Fabregat J. (eds.) IAU Colloq. 175: The Be Phenomenon in Early-Type Stars. ASP Conf. Ser. 214, Astron. Soc. Pacific, San Francisco, p. 656

Compton A.H., 1923, Phys. Rev. 21, 483

Cooley J.W., Tukey J.W., 1965, Mathematics of Computation 19, 297

Corbel S., Coriat M., Brocksopp C., et al., 2013, MNRAS 428, 2500

Dove J.B., Wilms J., Nowak M.A., et al., 1998, MNRAS 298, 729

Ebisawa K., Yamauchi S., Tanaka Y., et al., 2007, Progress of Theoretical Physics Supplement 169, 121

Fender R.P., Belloni T.M., Gallo E., 2004, MNRAS 355, 1105

Fender R.P., Homan J., Belloni T.M., 2009, MNRAS 396, 1370

Fender R.P., Maccarone T.J., Heywood I., 2013, MNRAS 430, 1538

Fourier J., 1822, Théorie analytique de la chaleur, Chez Firmin Didot, père et fils

Frank J., King A., Raine D.J., 2002, Accretion Power in Astrophysics: Third Edition, Cambridge University Press

Friend D.B., Castor J.I., 1982, ApJ 261, 293

Fürst F., Suchy S., Kreykenbohm I., et al., 2011, A&A 535, A9

Gallo E., Marolf D., 2009, American Journal of Physics 77, 294

Gauss C.F., 1866, Nachlass: Theoria interpolationis methodo nova tractata. In: Werke, Vol. 3. Königliche Gesellschaft der Wissenschaften, Göttingem, p.265

Grinberg V., 2013, Ph.D. thesis, Friedrich Alexander Universität Erlangen-Nürnberg

Grupen C., Shwartz B., 2008, Particle Detectors, Cambridge University Press

Haardt F., Maraschi L., 1991, ApJ 380, L51

Hanke M., 2011, Ph.D. thesis, Friedrich Alexander Universität Erlangen-Nürnberg

Hardcastle M.J., 2005, A&A 434, 35

Haswell C.A., King A.R., Murray J.R., Charles P.A., 2001, MNRAS 321, 475

Heindl W.A., Smith D.M., 2002, ApJ 578, L125

Helmert F.R., 1876, Zeitschrift für Mathematik und Physik 21, 102

Houck J.C., 2002, In: Branduardi-Raymont G. (ed.) High Resolution X-ray Spectroscopy with XMM-Newton and Chandra.

Houck J.C., Denicola L.A., 2000, In: Manset N., Veillet C., Crabtree D. (eds.) Astronomical Data Analysis Software and Systems IX. ASP Conf. Ser. 216, Astron. Soc. Pacific, San Francisco, p. 591

Iping R.C., Petterson J.A., 1990, A&A 239, 221

Jahoda K., Markwardt C.B., Radeva Y., et al., 2006, ApJS 163, 401

Jahoda K., Swank J.H., Giles A.B., et al., 1996, In: O. H. Siegmund & M. A. Gummin (ed.) EUV, X-Ray, and Gamma-Ray Instrumentation for Astronomy VII. SPIE Conf. Ser. 2808, p.59

Kalberla P.M.W., Burton W.B., Hartmann D., et al., 2005, A&A 440, 775

Klein O., Nishina T., 1929, Zeitschrift für Physik 52, 853

Kühnel M., 2011, *Master's thesis*, Friedrich Alexander Universität Erlangen-Nürnberg

Lagrange J.L., 1772, Prix de l'Académie Royale des Sciences de Paris tome IX

Leahy D.A., Darbro W., Elsner R.F., et al., 1983a, ApJ 266, 160

Leahy D.A., Elsner R.F., Weisskopf M.C., 1983b, ApJ 272, 256

Levine A.M., Bradt H., Cui W., et al., 1996, ApJ 469, L33

Lightman A.P., White T.R., 1988, ApJ 335, 57

Lightman A.P., Zdziarski A.A., 1987, ApJ 319, 643

Lomb N.R., 1976, Ap&SS 39, 447

Lubow S.H., 1991a, ApJ 381, 259

Lubow S.H., 1991b, ApJ 381, 268

Lynden-Bell D., 1969, Nature 223, 690

Magdziarz P., Zdziarski A.A., 1995, MNRAS 273, 837

Maloney P.R., Begelman M.C., 1997, ApJ 491, L43

Maloney P.R., Begelman M.C., Nowak M.A., 1998, ApJ 504, 77

Maloney P.R., Begelman M.C., Pringle J.E., 1996, ApJ 472, 582

Mandrou P., 1990, IAU Circ. 5032, 1

Markoff S., Nowak M.A., Wilms J., 2005, ApJ 635, 1203

Marti J., Mereghetti S., Chaty S., et al., 1998, A&A 338, L95

Masetti N., Bianchini A., Bonibaker J., et al., 1996, A&A 314, 123

Matt G., Perola G.C., Piro L., Stella L., 1992, A&A 257, 63

Miniutti G., Fabian A.C., Anabuki N., et al., 2007, PASJ 59, 315

Miyamoto S., Kitamoto S., Iga S., et al., 1992, ApJ 391, L21

Motta S., Belloni T., Homan J., 2009, MNRAS 400, 1603

Muñoz-Arjonilla A.J., Martí J., Luque-Escamilla P.L., et al., 2010, A&A 519, A15

Naik S., Paul B., 2004, A&A 418, 655

Neilsen J., Hickox R.C., Vrtilek S.D., 2004, ApJ 616, L135

Newton I., 1730, Opticks: Or, A Treatise of the Reflections, Refractions, Inflections and Colours of Light, W. Innys

Noble M.S., Nowak M.A., 2008, PASP 120, 821

Nowak M.A., Hanke M., Trowbridge S.N., et al., 2011, ApJ 728, 13

Nyquist H., 1928, Trans. Am. Inst. El. Engineers 47, 617

Obst M., 2011, *Bachelor's thesis*, Friedrich Alexander Universität Erlangen-Nürnberg

Ogilvie G.I., Dubus G., 2001, MNRAS 320, 485

Oppenheimer J.R., Snyder H., 1939, Phys. Rev. 56, 455

Oppenheimer J.R., Volkoff G.M., 1939, Phys. Rev. 55, 374

Oskinova L.M., Feldmeier A., Kretschmar P., 2013, In: Zhang C.M., Belloni T., Méndez M., Zhang S.N. (eds.) Feeding Compact Objects: Accretion on All Scales. IAU Symposium 290, Cambridge University Press, p.287

Parseval des Chênes M.A., 1806, Mémoires présentés à l'Institut des Sciences, Lettres et Arts, par divers savans, et lus dans ses assemblées. Sciences, mathématiques et physiques. (Savans étrangers.) 1, 638

Petterson J.A., 1977, ApJ 216, 827

Poisson S., 1837, Recherches sur la probabilité des jugements en matière criminelle et en matière civile: précédées des règles générales du calcul des probabilités, Bachelier

Pottschmidt K., 2002, Ph.D. thesis, Universität Tübingen

Pottschmidt K., Chernyakova M., Lubiński P., et al., 2008, In: Proceedings of "An INTEGRAL view of compact objects" – 7th INTEGRAL Workshop., PoS, id.67

Press W.H., Rybicki G.B., 1989, ApJ 338, 277

Press W.H., Teukolsky S.A., Vetterling W.T., Flannery B.P., 1992, Numerical recipes in FORTRAN. The art of scientific computing, Cambridge University Press, 2nd ed.

Pringle J.E., 1996, MNRAS 281, 357

Remillard R.A., 2005, In: P. Chen, E. Bloom, G. Madejski, & V. Patrosian (ed.) 22nd Texas Symposium on Relativistic Astrophysics., p.79

Remillard R.A., McClintock J.E., 2006, ARA&A 44, 49

Reynolds A.P., Hilditch R.W., Bell S.A., Hill G., 1993, MNRAS 261, 337

Roche É., 1849, Académie des sciences de Montpellier: Mémoires de la section des sciences 1, 243

Roche É., 1850, Académie des sciences de Montpellier: Mémoires de la section des sciences 1, 333

Roche É., 1851, Académie des sciences de Montpellier: Mémoires de la section des sciences 2, 21

Rodriguez L.F., Mirabel I.F., Marti J., 1992, ApJ 401, L15

Rothschild R.E., Blanco P.R., Gruber D.E., et al., 1998, ApJ 496, 538

Rothstein D.M., Eikenberry S.S., Chatterjee S., et al., 2002, ApJ 580, L61

Runge C., 1903, Zeitschrift für Mathematik und Physik 48, 554

Runge C., 1905, Zeitschrift für Mathematik und Physik 53, 1

Rybicki G.B., Lightman A.P., 1979, Radiative processes in astrophysics, New York, Wiley-Interscience

Sako M., Liedahl D.A., Kahn S.M., Paerels F., 1999, ApJ 525, 921

Scargle J.D., 1982, ApJ 263, 835

Schwarzenberg-Czerny A., 1989, MNRAS 241, 153

Shakura N.I., Sunyaev R.A., 1973, A&A 24, 337

Shannon C.E., 1949, Proceedings of the IRE 37, 10

Smak J., 1982, Acta Astronomica 32, 213

Smith D.M., Heindl W.A., Markwardt C.B., Swank J.H., 2001, ApJ 554, L41

Smith D.M., Heindl W.A., Swank J.H., 2000, In: AAS/High Energy Astrophysics Division #5, Vol. 32. BAAS, p. 1234

Smith D.M., Heindl W.A., Swank J.H., 2002, ApJ 569, 362

Smith I.A., 2010, In: AAS/High Energy Astrophysics Division #11, Vol. 42. Bulletin of the American Astronomical Society, p.671

Soria R., Broderick J.W., Hao J., et al., 2011, MNRAS 415, 410

Sundqvist J.O., Owocki S.P., 2013, MNRAS 428, 1837

Syunyaev R., Gilfanov M., Churazov E., et al., 1991, Sov. Astron. Let. 17, 50

Tananbaum H., Gursky H., Kellogg E., et al., 1972, ApJ 177, L5

Timmer J., Koenig M., 1995, A&A 300, 707

Titarchuk L., 1994, ApJ 434, 570

van der Klis M., 1989, In: H. Ögelman & E. P. J. van den Heuvel (ed.) Timing Neutron Stars., Kluwer Academic / Plenum Publishers, New York, p.27

Warner B., 2003, Cataclysmic Variable Stars, Cambridge University Press

Whitehurst R., 1988, MNRAS 232, 35

Whitehurst R., King A., 1991, MNRAS 249, 25

Wijers R.A.M.J., Pringle J.E., 1999, MNRAS 308, 207

Wilms J., Nowak M.A., Pottschmidt K., et al., 2001, MNRAS 320, 327

Wojdowski P., Clark G.W., Levine A.M., et al., 1998, ApJ 502, 253

Zdziarski A.A., 1985, ApJ 289, 514

Zhang W., Giles A.B., Jahoda K., et al., 1993, In: Siegmund O.H. (ed.) EUV, X-Ray, and Gamma-Ray Instrumentation for Astronomy IV, Vol. 2006. SPIE Conf. Ser., p.324

Acknowledgments

First of all, I want to thank my advisor, Jörn Wilms, who not only gave me opportunity to do research from the very beginning of my studies and always listened to (or read my emails ;-)) and motivated me, but without whose continuing support I would not have been able to make the wonderful experience of having a child while still studying.

My thanks goes to him and all my colleagues Anne, Fe, Mina, Basti, Michael, Thomas and Tobi, Thorsten and all other Remeisen who did not mind me bringing Jaan to work with me, leaving early or staying whole days at home. Discussions with you, in Erlangen as well as in Bamberg and on the way in-between gave me a lot of help and input. Especially Thomas, Fritz and Ingo, who take care of the Remeis cluster, made my work much easier and helped me solve all computer related problems. In this context, I also want to thank all contributors to the `isisscripts` provided by ECAP/Remeis observatory and MIT (http://www.sternwarte.uni-erlangen.de/isis/), as well as John E. Davis for the development of the SLxfig module which was used to create all the figures.

Thanks also goes to the Black Hole Telecon gang for scheduling telecons compatible with daycare times and for continuous discussions on various scientific topics. In particular I want to thank Katja, Victoria, David, John and Arash as well as my other co-authors Anne, Marion, Natalie, Fe, Ingo and Bárbara for many questions and comments and input on the ongoing work.

Special thanks goes to Natalie who, whichever time zone difference there was between us, always listened and answered questions of every (and not only scientific) kind. The many Skype and personal discussions gave me much to think about and helped a lot to sort and extend my ideas.

And finally, without words where words are insufficient anyway, my parents, my husband Heiko and my son Jaan:

Thank you!

Erklärung

Hiermit bestätige ich, dass ich diese Arbeit selbstständig und nur unter Verwendung der angegebenen Hilfsmittel angefertigt habe.

Erlangen, 29.01.2014

Maria Hirsch